Atmospheric Research 302 (2024) 107304

Contents lists available at ScienceDirect

Atmospheric Research

journal homepage: www.elsevier.com/locate/atmosres

Comparing the mechanisms of two types of summer extreme precipitation in Beijing-Tianjin-Hebei region, China: Insights from circulation patterns and moisture transports

Jing Cong [a,d], Huijun Liu [c,e], Guicai Ning [b,*], Hong Chen [a,d], Xueyan Bi [f], Bo Liu [a,d], Yuanjian Yang [b], Haiyun Xia [b]

[a] Tianjin Meteorological Observatory, Tianjin 300074, China
[b] Collaborative Innovation Centre on Forecast and Evaluation of Meteorological Disasters, School of Atmospheric Physics, Nanjing University of Information Science & Technology, Nanjing 210044, China
[c] Fujian Key Laboratory of Severe Weather, Fuzhou 350028, China
[d] Tianjin Key Laboratory for Oceanic Meteorology, Tianjin 300074, China
[e] Fujian Provincial Meteorological Observatory, Fuzhou 350028, China
[f] Guangzhou Institute of Tropical and Marine Meteorology, China Meteorological Administration, Guangzhou 510080, China

ARTICLE INFO

Keywords:
Extreme precipitation
Circulation patterns
Moisture transports
Return periods
Long-term trends
Beijing-Tianjin-Hebei

ABSTRACT

Beijing-Tianjin-Hebei (BTH) is undergoing huge risks from severe precipitation extremes, but their climate features and underlying mechanisms are not fully understood and warrant in-depth investigations. Here, the summer extreme precipitation events in BTH are objectively divided into two types according to the spatial distribution i.e., Northeast precipitation (*NEP*) and Southwest precipitation (*SWP*) and their underlying mechanisms are revealed and compared from perspectives of circulation patterns and moisture transports. In the case of *Type NEP*, the anomalous deep low-pressure (high-pressure) systems respectively cover over the west (east) of BTH, which jointly induce strong anomalous southwesterly and southerly airflows converging over BTH. The converging airflows strengthen water vapor transports from the western and southern boundaries of BTH and result in a strong convection over northeastern BTH, thereby triggering *Type NEP* precipitation. Compared with *Type NEP*, the circulation pattern of *Type SWP* is characterized by an anomalous deep (shallow) high-pressure (low-pressure) system over northeast (southwest) of BTH, respectively. The circulation patterns could induce strong anomalous southerly and easterly airflows converging over BTH and thus strengthen water vapor transports from the southern and eastern boundaries of BTH, resulting in a strong convection over southwestern BTH. Over the long-term period, the summer extreme precipitation days with multiple return periods extracted by the Generalized extreme value distribution theory show significantly increasing trends in Beijing-Tianjin and surrounding areas, particularly in urban regions, indicating that summer extreme precipitation events are becoming more frequent. These findings provide theoretical basis for summer extreme precipitation forecasting and scientific insight for taking effective measures to mitigate the corresponding disasters in BTH.

1. Introduction

Under the background of climate warming, weather and climate extremes occur frequently, posing harmful impacts on societal and ecological systems (Easterling et al., 2000; IPCC, 2021; Zaz et al., 2019). Climate warming can modulate the water cycle by strengthening surface water vapor evaporation and thus poses significant effects on global precipitation (Jin, 2014; Rawlins et al., 2010; Westra et al., 2013). In China, extreme precipitation events are particularly sensitive (Xu et al., 2009) and more responsible to climate warming (Sun et al., 2020; Wu et al., 2015), causing huge disasters such as floods and urban waterlogging (Sun and Zhang, 2017; Zhai et al., 2005; Quan, 2014; Donat et al., 2016; Zaz et al., 2019). As global warming continues, it is noteworthy that extreme precipitation will occur more frequently (Long et al., 2016) and exhibit more and more strong precipitation intensity (Zhang and Zhou, 2020; Wu et al., 2015). Investigating the climate

* Corresponding author.
E-mail addresses: guicaining@hotmail.com, 003746@nuist.edu.cn (G. Ning).

https://doi.org/10.1016/j.atmosres.2024.107304
Received 2 November 2023; Received in revised form 17 February 2024; Accepted 20 February 2024
Available online 21 February 2024

features and underlying mechanism of extreme precipitation is therefore urgently needed to provide scientific insights for taking adaptation measures to mitigate the relevant disasters.

Extreme precipitation is significantly modulated by atmospheric circulations and varies across different areas (Ning et al., 2021; Huang et al., 2017). In East China, summer extreme precipitation is affected by the weak East Asian summer monsoon (EASM) and the southerly strong western Pacific subtropical high (WPSH) (Wang and Zhou, 2005; Qian et al., 2009; Lu et al., 2004), which can bring abundant water vapor from the South China sea and western Pacific and provide favorable dynamic conditions (Li, 2011). On the contrary, summer extreme precipitation in North China is controlled by the circulation pattern of western low-pressure and eastern high-pressure system (Chen, 2012; Liu et al., 2007), accompanying with water vapor transport by strengthened EASM (Ding, 1992; Li and Zhou, 2015) and northward-extended WPSH (Wang and Zhou, 2005). In particular in the Xinjiang of Northwest China, a wave pattern with the deepening of the western Siberian trough, central Asian high, and Mongolian high are the main weather systems causing summer precipitation events, which can transport a large amount of water vapor and induce a strong convection over here (Ning et al., 2021; Zhou et al., 2021; Wang et al., 2019). What's more, the downstream development effect of the wave pattern originating from the northeast side of the Tibetan plateau also triggers extreme precipitation occurrence in Central China (Saeed et al., 2011). These studies reveal the underlying mechanism of extreme precipitation by investigating the physical processes of extreme precipitation as a whole for all extreme precipitation events and highlight that the atmospheric circulations significantly modulate extreme precipitation by transporting water vapor and providing convective conditions.

Beijing-Tianjin-Hebei (BTH), as the most core areas of China, is located in the North China Plain, which has large population density and the most active economic development in China and faces with more and more frequent and intense extreme precipitation (Guo et al., 2019; Liang et al., 2018). In BTH, rainfall mainly occurs in summer with mean annual summer precipitation of 343.6 mm during 1979 to 2020. Especially during July to August, rainstorms (the 24 h accumulated precipitation $\geq$ 50 mm) are characterized by strong suddenness frequently occurring and often induce several extreme precipitation events (Yu et al., 2015). These extreme precipitation events may exert more serious damages to human health, societal, and ecological systems. For instance, the extreme precipitation event occurred in Beijing and its surrounding areas in July 21, 2012 with the regional average precipitation of 190.3 mm in Beijing (Chen et al., 2012). The amount of precipitation at 8 national meteorological stations in Beijing and its surrounding areas broke their records and this rainstorm events results in 1.9 million people suffering disasters, 112 human deaths and a large economic loss of $>$ 10 billion RMB (Chen et al., 2012; Du et al., 2014). During July, 20 to 21, 2016, an extreme precipitation event occurred in BTH and induced the amount of precipitation at 70 meteorological stations exceeding 400 mm, resulting in disaster to 14.76 million people, 164 deaths, and 31.14 billion RMB in economic losses (Kang, 2017). Therefore, it is of great significance for disaster prevention and mitigation to reveal the climate features and physical mechanism of extreme precipitation in BTH as it could provide a theoretical basis for improving forecast skill of weather extremes.

There are two definitions of extreme climate, one is based on the definition of extreme index (Hartmann and Buchanan, 2014; Ning et al., 2021), and the other is based on the definition of extreme value theory (Seneviratne et al., 2012). Although the definition of extreme index including relative threshold method has widely used in climate extremes, the chosen extreme precipitation events represent 'the normality of extreme values' (Li and Yang, 2015) and are not enough to capture the most extreme climate condition. In contrast, extreme value theory is used to investigate more intense extreme events whose probability are more extreme than any that have already been observed (Liu, 2022; Coles, 2001). In this study, we therefore firstly apply the Generalized extreme value (GEV) method for exploring the spatio-temporal variations of summer extreme precipitation with multiple return periods in BTH. Then, the regional summer extreme precipitation events in BTH are divided into different types according to the spatial distribution by K-means clustering method. Finally, the underlying mechanisms of different types of extreme precipitation are investigated from the atmospheric circulation and moisture transport perspectives. However, most of existing studies revealed underlying mechanism of extreme precipitation by examining the physical processes of all extreme precipitation events as a whole, rather than performing cluster analysis. Thus, our study is expected to get some new scientific insights for predicting extreme precipitation and taking effective measures to mitigate the corresponding disasters in BTH region.

2. Data and method

2.1. Data

In this study, we mainly investigate the summer extreme precipitation (June to August) during 1979 to 2020 in BTH region. The daily precipitation on national meteorological stations in BTH is directly obtained and downloaded from the website (http://10.226.89.55/cimissapiweb/) developed by China Meteorological Administration (CMA). To ensure the quality of the raw data, we firstly remove the national meteorological stations with any three or more summers that have $>$ 3 missing days and 172 stations are retained for the subsequent analysis (Fig. 1). Notably, the urban areas have been marked in Fig. 1 to briefly discuss the impact of urbanization on extreme precipitation events in BTH. As shown in Fig. 1, we find that 32 stations are located in urban areas and the proportion of urban stations to total stations is about 18.6%.

The ERA5 hourly reanalysis data are used to investigate the underlying mechanism of extreme precipitation in BTH, which covers the period from 1950 to now with the highest spatial resolution of 0.25° $\times$ 0.25° (Hersbach et al., 2020). We have obtained atmospheric variables including surface pressure, 2 m temperature and horizontal wind, geopotential height, upper horizontal wind, vertical velocity, specific humidity, and their derivative variables such as divergence, moisture flux and moisture flux divergence. The pressure levels taking for the tropospheric analysis are 1000 hPa, 925 hPa, 850 hPa, 800 hPa, 700 hPa, 600 hPa, 500 hPa, 400 hPa, 300 hPa, 250 hPa, 200 hPa, 100 hPa, 50 hPa. All these variables are calculated to daily data by calculating averaged value of 24-hourly data with the spatial resolution of 0.25° $\times$ 0.25°.

2.2. Methodology

In this study, the four models of GEV distribution theory including one stationary and three non-stationary models are selected to identify summer extreme precipitation events with 5–50 years return periods on each station in BTH. Then, the long-term trends of the summer extreme precipitation events with 5–50 years return periods are examined by the Mann-Kendall test. Notably, we also define a method for identifying the regional summer extreme precipitation event and thus a total of 43 regional summer extreme precipitation events with 5 years return period are identified in BTH. According to the K-means clustering method, the 43 events are divided into two types and finally the underlying mechanisms of the two types of extreme precipitation are investigated by the composite analysis method from the perspectives of atmospheric circulations and moisture transport. The workflow chart of the above methodology is shown in Fig. S1.

2.2.1. GEV distribution theory

Extreme value theory is an effective method to select extreme climate events in the limited samples (Zwiers et al., 2011). As one of the most important tools of extreme value theory (Liu, 2022), the GEV distribution theory has been widely used in statistical analysis of annual extreme

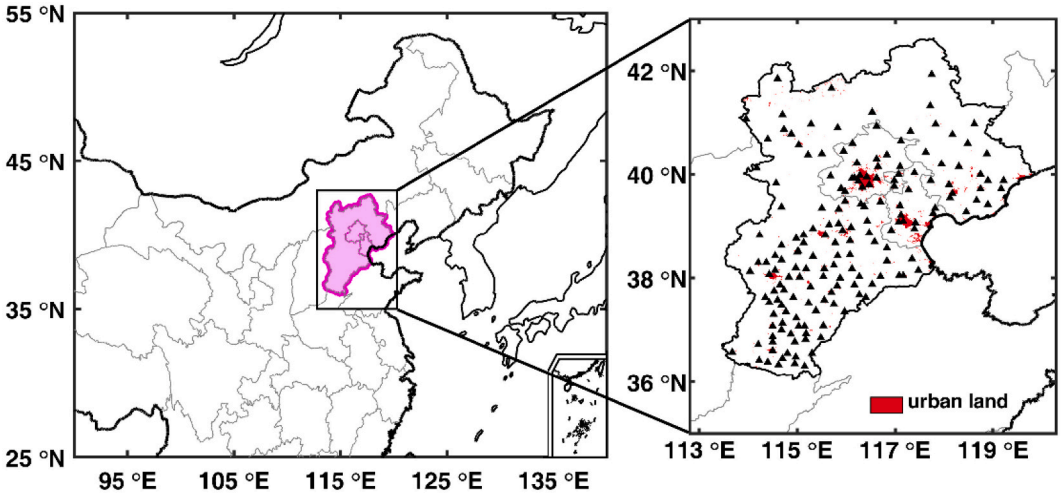

Fig. 1. The map of Beijing-Tianjin-Hebei region (the purple filled area). The red filled areas in the right figure indicate urban areas and the solid dots (triangles) representing the national meteorological stations located in non-urban (urban) areas. (For interpretation of the references to colour in this figure legend, the reader is referred to the web version of this article.)

values' series in meteorological, hydrological, and other fields (Coles, 2001). In detail, the GEV cumulative density function (CDF) is fitted the annual extreme values distribution and the extreme climate are defined when daily value is over (or below) some threshold in the upper (or lower) tail of GEV CDF (Liu, 2022). The extreme climate events with any return period of T are actually referred to daily meteorological observed values over threshold determined by the probability of occurrence $1–1/T$ on GEV CDF (Liu, 2022; Tu et al., 2022). The GEV CDF is shown as below Eq. (1).

$$G(x) = \begin{cases} exp\left\{ -\left[1+\xi\frac{x-\mu}{\sigma}\right]^{-\frac{1}{\xi}}\right\}, \xi \neq 0 \\ exp\left\{ -exp\left(-\frac{x-\mu}{\sigma}\right)\right\}, \xi = 0 \end{cases} \quad (1)$$

The GEV distribution is determined by the location parameter μ; scale parameter σ and shape parameter ξ. Assuming $G(x) = 1-p$, the extreme quantiles z_p of the annual maximum distribution could be obtained by inverting Eq. (2).

$$z_p = \begin{cases} \mu - \frac{\sigma}{\xi}\left\{\left[1-[-log(1-p)]^{-\xi}\right\}, \xi \neq 0 \\ \mu - \sigma log[-log(1-p)], \xi = 0 \end{cases} \quad (2)$$

z_p is the return level associated with the return period $1/p$, which is expected on average once every $1/p$ years. More details can be found in Coles (2001).

The GEV distribution is stationary when parameters μ, $\sigma$and ξ are constants. In contrast, the GEV distribution is non-stationary if anyone parameters μ, σ or ξ is non-constant. The shape parameter is often stable constant (Tu et al., 2022; Li and Zhou, 2015), and the location and scale parameters μ, σ are respectively defined in Eqs. (3)–(4), as follows (Tu et al., 2022).

$$\mu_t = \alpha_0 + \alpha_1 t \quad (3)$$

$$log\sigma_t = \beta_0 + \beta_1 t \quad (4)$$

Where, t is time variable. Four models could be fitted to the series of annual precipitation maxima as below:

$M_0 : \alpha_1 = 0, \beta_1 = 0$, describing a stationary model.

$M_1 : \alpha_1 \neq 0, \beta_1 = 0$, describing a non-stationary model on the location parameter.

$M_2 : \alpha_1 = 0, \beta_1 \neq 0$, describing a non-stationary model on the scale parameter.

$M_3 : \alpha_1 \neq 0, \beta_1 \neq 0$, describing a non-stationary model on both two parameters.

In this study, the above four types of models (M_0–M_3) have been tested on each station in BTH by the ismev package of R language (Stephenson, 2018; Coles, 2001). To avoid multiple comparing the maximum likelihood Ratio difference between each model, we use the Akaike's Information Criteria (AIC) to determine the optimum fitting model (Tu et al., 2022). AIC (Akaike, 1974) is calculated by following Eq. (5).

$$AIC(k) = 2nllh(k) + 2k \quad (5)$$

Where, k is freedom degree of the model, $nllh$ is negative loglikelihood. The optimum fitting model is finally determined when the mode has the minimal AIC.

The optimum fitting distribution judged by AIC on each station of BHT is shown in Fig. S2. We find that the stationary model of M_0 is the most suitable model at 150 stations (87.2% of the total stations in BTH) among the four fitted models, while the non-stationary model of M_1 and M_2 are the most models at 14 stations (8.1%) and 8 stations (4.7%), respectively. This also confirms again that stationary GEV distribution is almost suit for fitting the series of the annual maximum daily precipitation, which is consistent with previous analysis (Li and Zhou, 2015).

Then, we obtain the daily precipitation thresholds of 5–50 years return periods on each national station according to the above chosen GEV model. Referring to the definition of regional rainstorm provided by China Meteorological Administration (Hong, 2020), a situation in which the summer daily precipitation amounts at least 5% of the national stations in BTH region exceed their corresponding thresholds of 5 years return period on the same day is defined as the regional summer extreme precipitation day. According to the definition method, a total of 43 regional summer extreme precipitation days are selected during 1979 to 2020 and you can find the details about these extreme precipitation events in Table 1.

2.2.2. K-means clustering method

Clustering method is an unsupervised machine learning method (Gao, 2020) for dividing data set into different groups, which makes the characteristics between the same clusters as similar as possible and makes the different clusters as different as possible (Darby, 2005; Jain et al., 1999). K-means clustering method is widely applied in data science as its conceptual and numerical simplicity, which organizes the clusters based on the Euclidean distance to the centroid by pre-set clustering number k and repeated iteration (Bernier et al., 2019). The specific principle is presented by MacQueen (1967). The most important

Table 1
The date of precipitation begining and the maximum recorded precipitation of two types of summer extreme precipitation events in BTH.

Northeast precipitation (NEP)		Southwest precipitation (SWP)	
Date of beginning of precipitation	The Region's maximum recorded precipitation (mm)	Date of beginning of precipitation	The Region's maximum recorded precipitation (mm)
1979/07/23	233.9	1980/06/28	237.3
1981/07/03	195.5	1981/08/14	179.6
1982/07/24	207.1	1981/08/15	273.5
1984/08/09	291	1982/07/30	165
1985/08/24	170.6	1984/08/08	214.8
1986/06/26	179.3	1987/08/25	234.2
1988/07/17	156.3	1989/07/16	163.9
1988/07/20	184.5	1990/08/25	206.2
1991/07/27	263.4	1993/08/03	302.6
1994/07/12	208.7	1994/07/11	260.2
1994/08/12	224.5	1996/07/09	221.8
1995/07/28	163.9	1996/08/03	413.3
1996/08/04	164.4	1999/08/08	138.7
1998/07/05	155.7	2000/07/03	165.2
2011/07/24	129.9	2000/07/04	201.5
2011/07/29	146.2	2000/07/05	194.7
2012/07/20	289	2001/07/26	143
2012/07/21	366.7	2004/07/11	237.5
2013/07/14	147.7	2005/07/22	311.4
2016/07/19	307.2	2015/08/02	181.8
2018/07/23	199.8	2016/07/18	273.3
2019/07/28	116.8		

step of K-means clustering method is to determine the optimal number of clusters. In this study, Calinski-Harabasz index, also known as the variance ratio criterion (VRC) (Caliński and Harabasz, 1974), is selected to determine the optimal number of clusters as reaching the maximum value of variance measurement ratio of homogeneity within a cluster to heterogeneity between clusters (Chikumbo and Granville, 2019; Łukasik et al., 2016). The Calinski-Harabasz index VRC is defined in Eq. (6).

$$VRC_k = \frac{SSB}{SSW} \times \frac{N-k}{k-1} \tag{6}$$

Where, SSB and SSW are respectively the overall variance between-clusters and the overall variance within-clusters as follows,

$$SSB = \sum_{i=1}^{k} n_i \|m_i - m\|^2 \tag{7}$$

$$SSW = \sum_{i=1}^{k} \sum_{x \in C_i} \|x - m_i\|^2 \tag{8}$$

Where, k is the number of clusters; N is the number of observations; n_i is number of observations in cluster i; m_i is the centroid of cluster i; m is the mean value of sample data; $\|m_i - m\|$ is L^2 norm (Euclidean distance); x is data point; c_i is cluster i; $\|x - m_i\|$ is L^2 norm (Euclidean distance) between the two vectors. In this study, the regional summer extreme precipitation events in BTH are finally divided into two clusters according to the Calinski-Harabasz index.

2.2.3. Calculation of water vapor budget

In order to explore the water vapor budget over the study region, we calculate integral of the whole layer moisture (from surface to 50 hPa) on the regional boundary (Li et al., 2019) as the net amount of water vapor. We define the water vapor flux incoming-flowing to the study region as positive amount and the water vapor flux out-flowing from the study region as negative amount. Thus, the cumulative amount of vertically integrated water vapor fluxes on the southern, northern, western, eastern boundaries are represented as the total water vapor budget over our study region, and the positive amount indicates increasing moisture and the negative value indicates decreasing moisture. The dimensions of the box constructed to calculate the inflow and outflow of moisture are from 113.25°E to 120°E, and from 36°N to 42.75°N. The detailed calculation formulas (Li et al., 2019) are shown below. The net total water vapor budget ($\overrightarrow{Q_T}$) over our study region is defined in Eq. (7).

$$\overrightarrow{Q_T} = \overrightarrow{Q_s} + \overrightarrow{Q_N} + \overrightarrow{Q_W} + \overrightarrow{Q_E} \tag{7}$$

Where, $\overrightarrow{Q_S}$, $\overrightarrow{Q_N}$, $\overrightarrow{Q_W}$, $\overrightarrow{Q_E}$ are the vertically integrated moisture fluxes on southern, northern, western, eastern boundaries and are respectively defined in Eqs. (8)–(11),

$$\overrightarrow{Q}_S = \int_{\lambda_W}^{\lambda_E} \overrightarrow{Q}_{\varphi_S} a cos\varphi_s d\lambda \tag{8}$$

$$\overrightarrow{Q}_N = \int_{\lambda_W}^{\lambda_E} \overrightarrow{Q}_{\varphi_N} a cos\varphi_N d\lambda \tag{9}$$

$$\overrightarrow{Q}_W = \int_{\varphi_S}^{\varphi_N} \overrightarrow{Q}_{\lambda_W} a d\varphi \tag{10}$$

$$\overrightarrow{Q}_E = \int_{\varphi_S}^{\varphi_N} \overrightarrow{Q}_{\lambda_E} a d\varphi \tag{11}$$

Where, λ_W (λ_E) is the longitude of each grid on western (eastern) boundary; φ_N (φ_S) is the latitude of each grid on northern (southern) boundary; a is the Earth radius; $\overrightarrow{Q}_{\varphi_S}$, $\overrightarrow{Q}_{\varphi_N}$, $\overrightarrow{Q}_{\lambda_W}$, $\overrightarrow{Q}_{\lambda_E}$ are the vertically integrated moisture flux at each grid on the boundaries and the formula of vertically integrated moisture flux is defined in Eq. (12),

$$\overrightarrow{Q} = \frac{1}{g} \int_{p_s}^{p_t} q \overrightarrow{v} d_p \tag{12}$$

Where, q is the specific humidity; $\overrightarrow{V}$ is the horizontal wind; p_s and p_t are respectively the surface pressure and the top layer (50 hPa).

2.2.4. Composite analysis method

The underlying physical mechanisms of two types of extreme precipitation are revealed and compared by investigating the composite anomalies of precipitation-related synoptic variables. Referring to the scheme on composite analysis in the previous studies (Luo et al., 2020; Luo and Lau, 2017; Ning et al., 2021), the daily anomalies of each synoptic variable are calculated by removing their climatological cycles before the composite analysis. Firstly, we average the synoptic variable at individual calendar days of the reference period of 1981–2010. Secondly, we perform a 31-day moving mean of the above averaged variable to get the climatological cycle of each synoptic variable. Thirdly, we calculate the daily anomalies of each synoptic variable by removing the above climatological cycle. Finally, we obtain the composite anomalies for each clustering type by averaging the daily anomalies of each variable on all days during the extreme precipitation events in this cluster. To guarantee statistical significance, we examine a significance test for the composite anomalies by the one-sample two-tail Student's t-test (Cressie, 1980). The test statistic t is calculated by Eq. (13).

$$t = \frac{\overline{x} - \mu}{\sigma_x / \sqrt{n}} \tag{13}$$

Where $\overline{x}$ is sample average; μ is the given mean; σ_x is sample standard deviation; n is the number of values in the sample. The degree of freedom is n-1.

The null hypothesis (H_0) is rejected if the p corresponding to t is less than the statistical significance level α, which means the sample average has obvious difference from the given mean. In this study, we procedure Student's t-test with sample size of 22 (21) on each station for *Type NEP* (*Type SWP*).

2.2.5. Mann-Kendall (MK) test

The Mann-Kendall test is a non-parametric trend test method, which

does not require the data to be normally distributed (Mann, 1945; Kendall, 1975) and could search for a trend without identify whether the trend is linear or nonlinear (Sang et al., 2014; Pingale et al., 2016). Thus, we select the Mann-Kendall test to examine the long-term trends of summer extreme precipitation frequency in BTH during 1979 to 2020. There has independent distributed time series $x(t)$ with the length of n and the null hypothesis is that the series has no trend (H_0). The statistic S in MK is defined in Eq. (14).

$$S = \sum_{i=1}^{n-1} \sum_{j=i+1}^{n} sgn(x(j) - x(i)) \tag{14}$$

With.

$$\begin{cases} sgn(x(j) - x(i)) = 1, x(j) - x(i) > 0 \\ sgn(x(j) - x(i)) = 0, x(j) - x(i) = 0 \\ sgn(x(j) - x(i)) = -1, x(j) - x(i) < 0 \end{cases} \tag{15}$$

It has been found that the statistic S is approximately normally distributed when $n > 8$ (Mann, 1945; Kendall, 1975) with the mean $E(S) = 0$ and variance $Var(S)$ as follows:

$$Var(S) = \frac{1}{18}\left[n(n-1)(2n+5) - \sum_{p=1}^{g} t_p(t_p - 1)(t_p + 5)\right] \tag{16}$$

Where t_p is the number of data in the tied group and g is the number of the tied groups.

The standardized MK test statistic Z can be estimated as follows:

$$Z = \begin{cases} (S-1)/\sqrt{Var(S)}, S > 0 \\ 0, S = 0 \\ (S+1)/\sqrt{Var(S)}, S < 0 \end{cases} \tag{17}$$

A positive (negative) value of Z indicates an upward (downward) trend. The null hypothesis of no trend (H_0) is rejected if $Z > Z_{1-\alpha/2}$, where α is the statistical significance level.

3. Results

3.1. Climatology features of extreme precipitation with different return periods

The GEV distribution theory is used to investigate the summer extreme precipitation thresholds with 5–50 years return periods on each meteorological station in BTH. The spatial distribution of extreme precipitation thresholds is depicted in Fig. 2. The extreme precipitation thresholds with 5–50 years return periods overall exhibit consistent spatial feature with a northwest-southeast increasing gradient distribution. Note that the high extreme precipitation thresholds especially with $>$ 20 years return period are more prominent in Beijing-Tianjin urban areas than those in rural areas (Fig. 2c–f), indicating that tremendously heavy precipitation events tend to occur in urban areas.

In addition, we also investigate the long-term trends of annual summer extreme precipitation frequency. As shown in Fig. 3, it is obvious that the summer extreme precipitation frequency exhibits significantly increasing trends in most areas of BTH, especially for the extreme precipitation with $>$ 10 years return period in Beijing-Tianjin and surrounding urban areas (Fig. 3c–f). On the contrary, the summer extreme precipitation frequency with $<$ 10 years return periods shows significantly decreasing trends in the southern and northeastern BTH (Fig. 3a–b). These results highlight that the long-term trends of annual summer extreme precipitation frequency exhibit distinct spatial differences and are closely related to the return periods, i.e., summer extreme precipitation in Beijing-Tianjin and surrounding urban areas becomes more and more frequent and the changing trends of summer extreme precipitation events with long-term return periods are more pronounced.

Overall, it is noteworthy that both the summer extreme precipitation

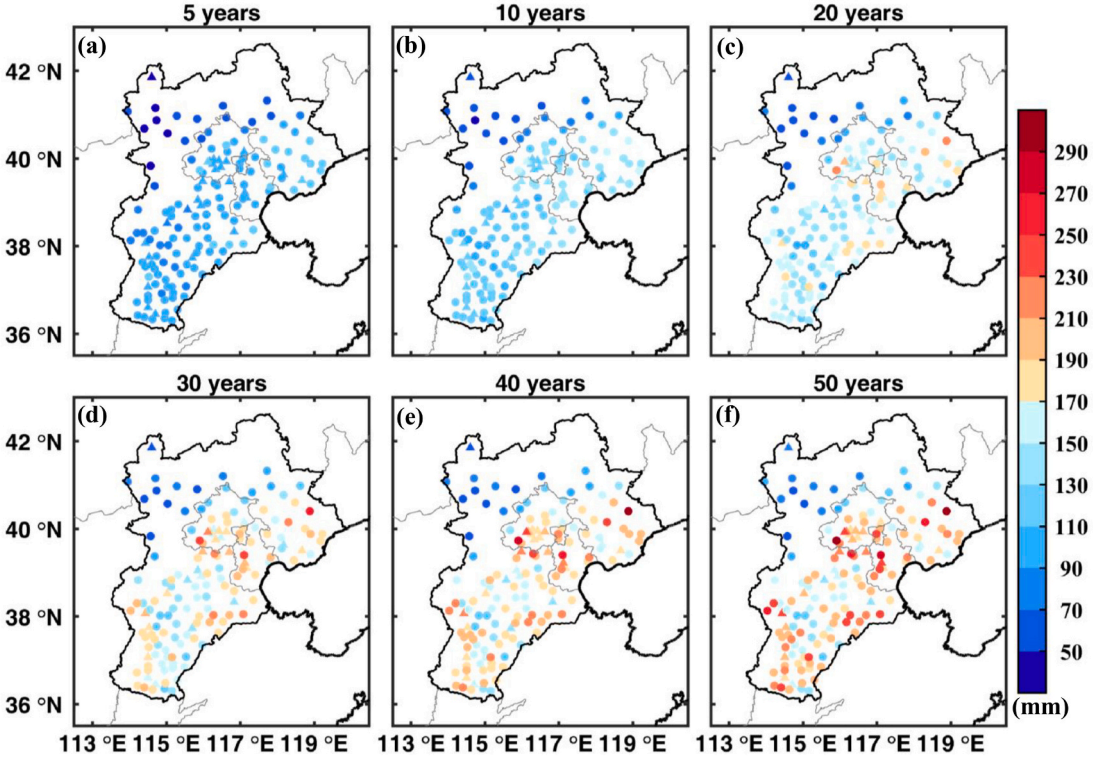

Fig. 2. The extreme precipitation thresholds (unit: mm) of (a) 5 years return period, (b) 10 years return period, (c) 20 years return period, (d) 30 years return period, (e) 40 years return period, (f) 50 years return period calculated by GEV distribution theory on national meteorological stations. The solid dots (triangles) representing the national meteorological stations located in non-urban (urban) areas.

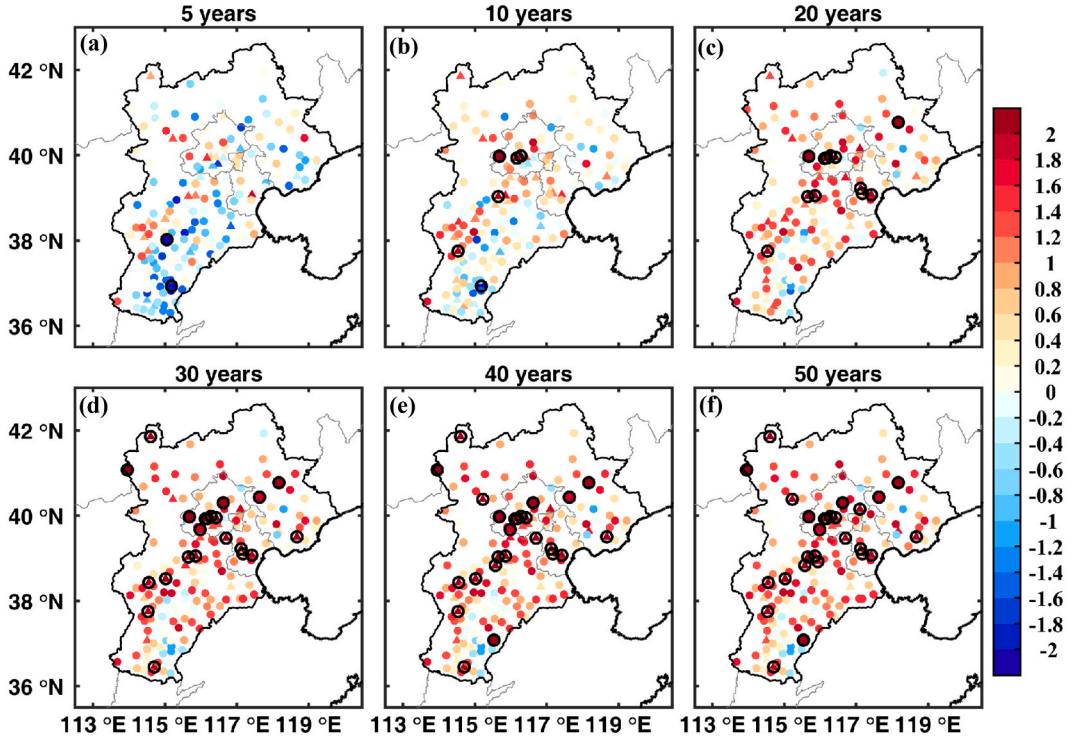

Fig. 3. The long-term trends of summer extreme precipitation frequency of (a) 5 years return period, (b) 10 years return period, (c) 20 years return period, (d) 30 years return period, (e) 40 years return period, and (f) 50 years return on national meteorological stations based on Mann-Kendall test. The positive (negative) values indicate increasing (decreasing) trends and the circle scattered points indicate that the trends are significant at the 0.05 level. The solid dots (triangles) representing the national meteorological stations located in non-urban (urban) areas.

thresholds and the increasing trends of summer extreme precipitation frequency with 5–50 years return periods are large in the Beijing-Tianjin and surrounding urban areas, suggesting that the summer extreme precipitation in the urban areas of BTH becomes stronger and more frequent in the past 42 years with climate warming. These results indicate that the urbanization may enhance the frequency and intensity of summer extreme precipitation in BTH, causing serious harm to people's lives and property as the high population density and developed economy in urban areas. Therefore, it is of great significance to investigate the climatology features and underlying physical mechanism of summer extreme precipitation in BTH.

3.2. *Clustering summer extreme precipitation according to its spatial distribution*

To comprehensively examine the climatology features and underlying physical mechanism of summer extreme precipitation in BTH region, the identified 43 regional summer extreme precipitation days with 5 years return period during 1979 to 2020 are clustered into two types by K-means clustering method. There is obvious difference in the spatial distribution among the two types of summer extreme precipitation, in particular for the position of precipitation center and the details are descripted as following. (1) *Type NEP*: the Northeast precipitation, whose rainstorm center (daily precipitation amount $\geq$ 50 mm) is located

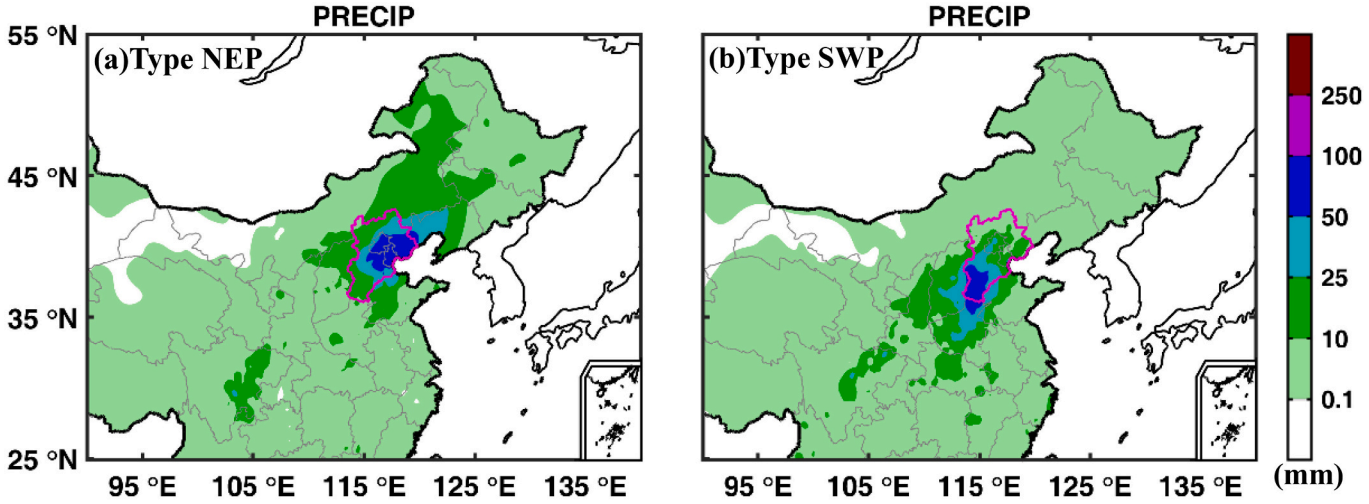

Fig. 4. Spatial distributions of the composite daily precipitation amount (unit: mm) of (a) *Type NEP* and (b) *Type SWP*. The boundary of BTH is indicated by the thick purple outline. (For interpretation of the references to colour in this figure legend, the reader is referred to the web version of this article.)

in the northeast region of BTH (Fig. 4a). (2) *Type SWP*: the Southwest precipitation, whose rainstorm center (daily precipitation amount $\geq$ 50 mm) is located in the southwest region of BTH (Fig. 4b). Note that each of the two types of summer extreme precipitation respectively accounts for 51.2% and 48.8% of the total extreme precipitation days, indicating that summer extreme precipitation events in BTH mainly consist by the two types of extreme precipitation. The date of beginning occurrence and the maximum recorded precipitation of two types of extreme precipitation are listed in Table 1.

3.3. Underlying physical mechanisms of two types of extreme precipitation

3.3.1. Near-surface characteristics of two types of extreme precipitation

Fig. 5 depicts the spatial distributions of the anomalies of precipitation, 2 m temperature, and surface pressure associated with the two types of summer extreme precipitation in BTH. Combining Fig. 5 and Fig. 4, we find that the spatial distributions of precipitation anomalies associated with *Type NEP* and *Type SWP* (Fig. 5a–b) are consistent with their spatial distributions of precipitation (Fig. 4), exhibiting significant positive anomalies of precipitation in most region of BTH. Note that the precipitation centers with anomalies > 60 mm show distinct difference between *Type NEP* and *Type SWP*, i.e., the precipitation center associated with *Type NEP* is located in the northeastern coastal area of BTH (Fig. 5a) while the center associated with *Type SWP* is located in the southwestern BTH (Fig. 5b). Under the cooling effect of precipitation, significant negative anomalies centers of temperature are also observed in the northeastern and southwestern BTH for the summer extreme precipitation of *Type NEP* and *Type SWP*, respectively (Fig. 5c–d). These result about cooling effect of precipitation is similar to existing studies about 2 m temperature under extreme precipitation in other regions, such as in arid Xinjiang of China (Ning et al., 2021).

We also examine the spatial distribution of the anomalies of surface pressure associated with the two types extreme precipitation. In the case of *Type NEP*, a significant strong anomalous low-pressure system and a significant strong high-pressure system respectively cover over BTH and

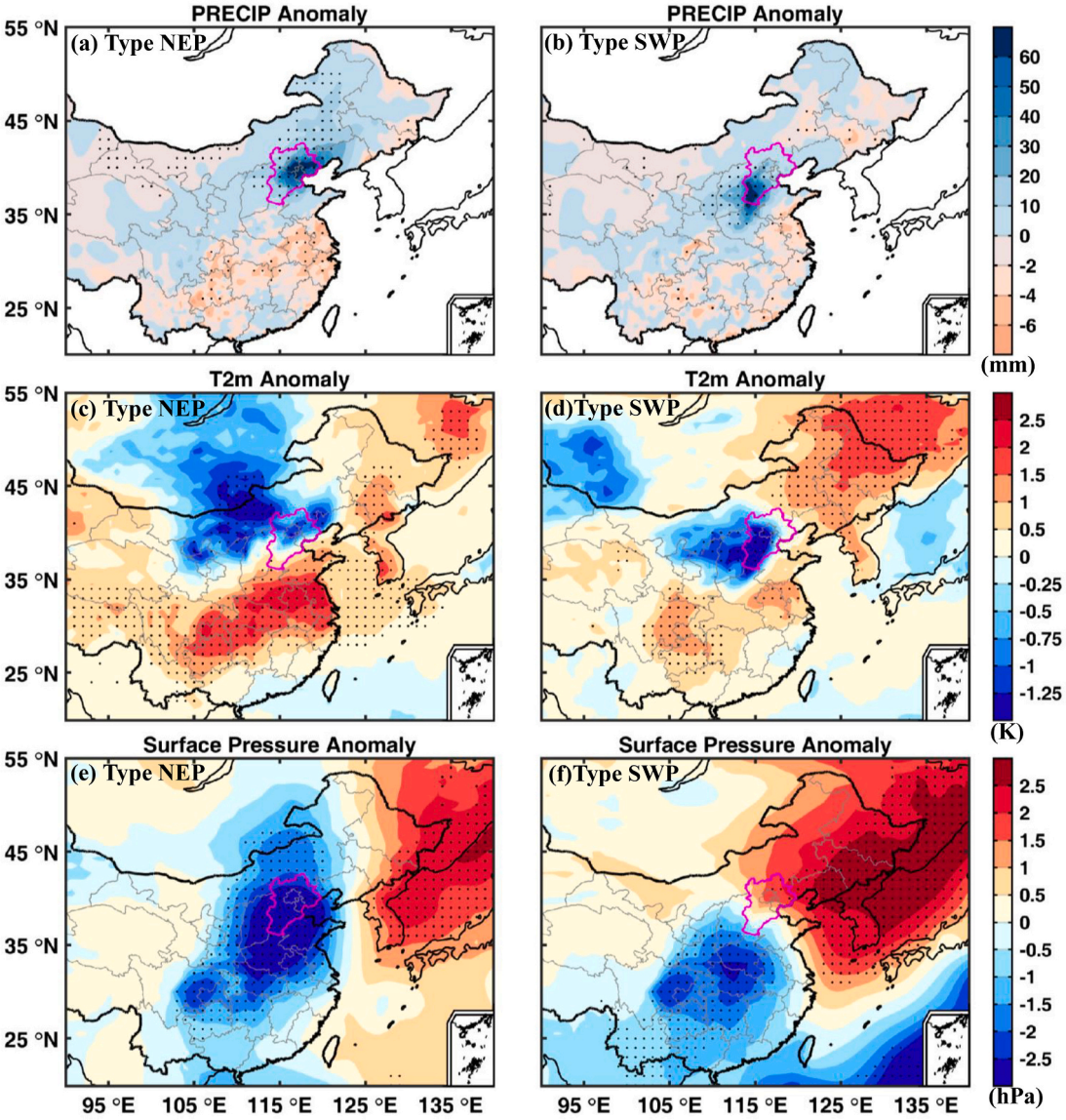

Fig. 5. Composite charts of the anomalies of precipitation (unit: mm), 2 m temperature (unit: K), and surface pressure (unit: hPa) associated with the two types of summer extreme precipitation in BTH. The left and right columns respectively show the anomalies associated with *Type NEP* and *Type SWP*. The top, middle, and bottom rows show the anomalies of precipitation, 2 m temperature, and surface pressure, respectively. Black scatter point indicates anomalies significant at the 0.05 level (two-tailed Student's *t*-test). The boundary of BTH is indicated by the thick purple outline. (For interpretation of the references to colour in this figure legend, the reader is referred to the web version of this article.)

oceanic region east of BTH (Fig. 5e), which induce convergence and transport large moisture over the northeastern BTH, providing favorable dynamical and moisture conditions for the occurrence and persistence of the *Type NEP* extreme precipitation. In contrast, the centers of the anomalous low-pressure system (high-pressure system) associated with Type SWP are respectively observed over the southwestward (northeastward) BTH (Fig. 5f), which induce convergence over the southwestern BTH, transporting sufficient moisture.

3.3.2. *Atmospheric conditions in the troposphere*

In order to examine the underlying physical mechanisms of the two types of summer extreme precipitation in BTH, the synoptic behaviors in troposphere are also investigated from perspectives of atmospheric circulations and moisture transport. The spatial distributions of the composite anomalies of geopotential height and wind vector in the upper-, middle-, and lower-troposphere associated with the two types of extreme precipitation are presented in Fig. 6 and Fig. 7. As shown in Fig. 6 and Fig. 7, the spatial distributions of the anomalies of geopotential height and wind vector exhibit obvious difference between *Type NEP* and *Type SWP*.

In the case of *Type NEP*, the anomalous low-pressure (high-pressure) system respectively covers over the west (east) of BTH, inclining eastward from the upper- to lower-troposphere (Fig. 6a, c, e). Notably, the strong eastern anticyclonic anomaly blocks the eastward movement of the western low-pressure anomaly in the middle- and lower-troposphere (Fig. 6c and e). As a result, the region of BTH controlled by the low-pressure system for a long time and thus triggering favorable dynamic conditions such as convergence and updraft (Fig. 5e and Fig. 6e), especially over the northeastern BTH. Moreover, the behaviors of the wind vector anomalies correspond well to the geopotential height. As shown in Fig. 7e, the anomalous southwesterly and southerly airflows converge in the front of low vortex at 850 hPa and constitute an obvious wind shear line, providing favorable dynamic conditions for the extreme precipitation of *Type NEP*. Notably, the significant anomalous southwesterly and southerly airflows are beneficial to transport a large amount of water vapor from South China and west of BTH to the

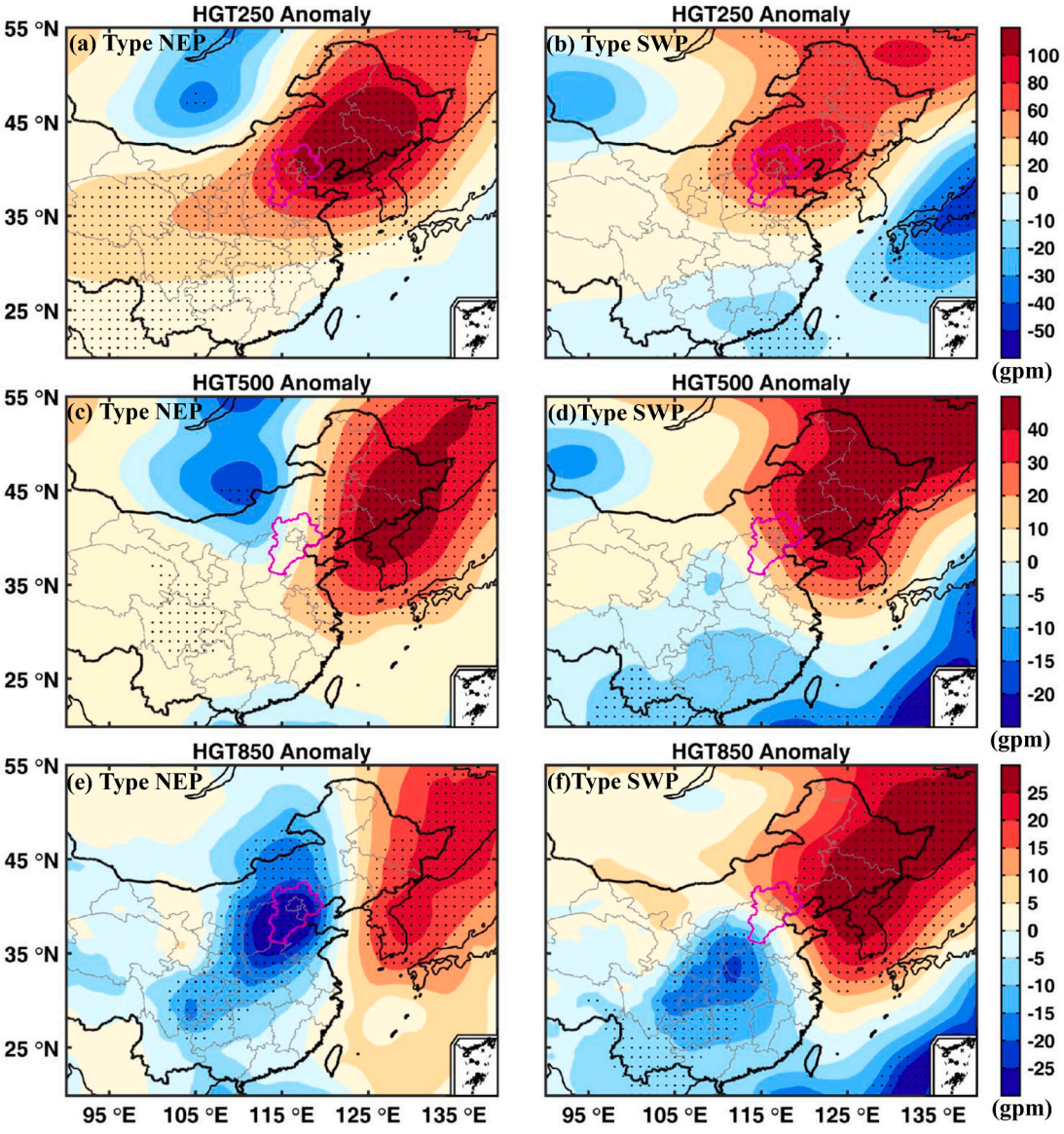

Fig. 6. Composite charts of the anomalies of geopotential height (unit: gpm) associated with the two types of summer extreme precipitation in BTH. The left and right columns respectively show the anomalies associated with *Type NEP* and *Type SWP*. The top, middle, and bottom rows show the anomalies at 250-, 500-, and 850 hPa, respectively. Black scatter point indicates anomalies significant at the 0.05 level (two-tailed Student's t-test). The boundary of BTH is indicated by the thick purple outline. (For interpretation of the references to colour in this figure legend, the reader is referred to the web version of this article.)

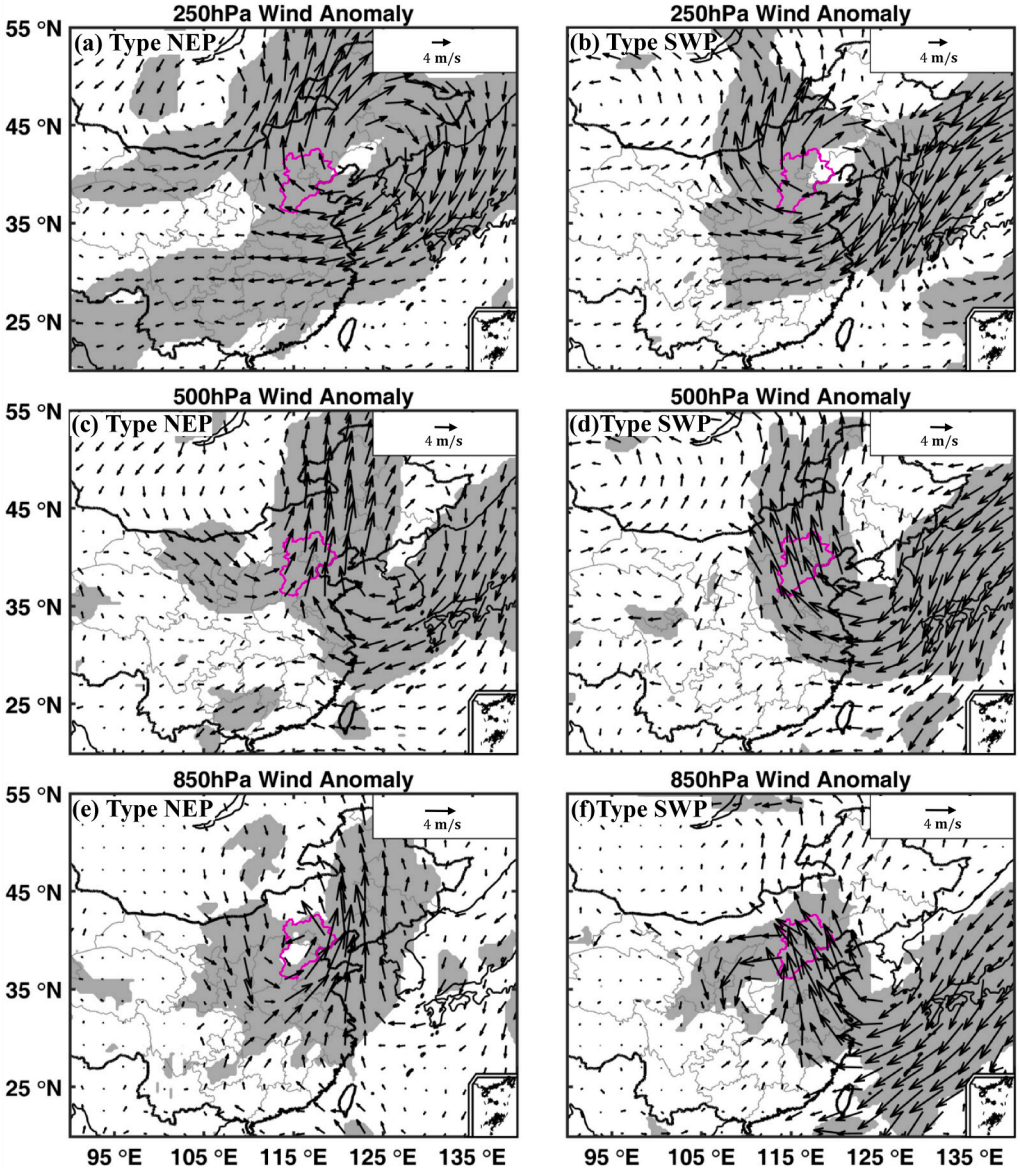

Fig. 7. Composite charts of the wind vector anomalies (unit: m/s) associated with the two types of summer extreme precipitation in BTH. The left and right columns respectively show the anomalies associated with *Type NEP* and *Type SWP*. The top, middle, and bottom rows show the anomalies at 250-, 500-, and 850 hPa, respectively. Black scatter point indicates anomalies significant at the 0.05 level (two-tailed Student's t-test). The boundary of BTH is indicated by the thick purple outline. (For interpretation of the references to colour in this figure legend, the reader is referred to the web version of this article.)

northeastern BTH (Xie and Ren, 2008; Zhou et al., 2008), supplying sufficient moisture for triggering extreme precipitation of *Type NEP*. It is noteworthy that under the effects of atmospheric circulations, a significant convergence center is observed in the lower-troposphere over the northeastern BTH, especially between 700 hPa and 925 hPa (Fig. 8c and e), while a significant divergence center appears in the upper-troposphere over the northeastern BTH at 250 hPa (Fig. 8a). The vertical distribution of lower-level convergence and upper-level divergence centers plays a key role in inducing the strong ascending motion by pumping action (Fig. 8a, c, e) (Huang et al., 2018a; Ahasan et al., 2013; Hu et al., 2018; Zhao et al., 2019), providing favorable dynamic conditions for triggering extreme precipitation of *Type NEP*.

Compared with *Type NEP*, atmospheric circulations in the upper- and middle-troposphere associated with *Type SWP* is only affected by a significant anomalous high-pressure system covering over the northeast of BTH (Fig. 6b and d). In the lower-troposphere, it is noteworthy that the anomalous low-pressure (high-pressure) system respectively covers over the southwest (northeast) of BTH (Fig. 6f). Compared with the *Type NEP*, the above two systems exhibit obvious differences in terms of their spatial locations and the anomalous low-pressure system located over the southwest of BTH becomes stronger from 850 hPa to surface (Fig. 6f and Fig. 5f). The spatial distribution of the wind vector anomalies also corresponds well to the geopotential height. In the lower-troposphere, the inverted trough wind shear is observed at the northeast boundary of the vortex system at 850 hPa (Fig. 7f) and could induce convergence and updraft motion over southwestern BTH, providing favorable dynamic conditions for the extreme precipitation of *Type SWP*. In addition, the anomalous southeasterly airflows could transport a large amount of water vapor from South China and the Northwest Pacific to the southwestern BTH, supplying sufficient moisture for triggering extreme precipitation of *Type SWP* (Yan, 2013; Zhao et al., 2019). It is also noteworthy that the vertical distribution of convergence and divergence associated with *Type SWP* is consistent with that of *Type NEP*. In short, the typical configuration of pumping action induced by the significant convergence at 925 hPa and the significant divergence at 250 hPa exactly corresponds to the position of rainstorm that located in the

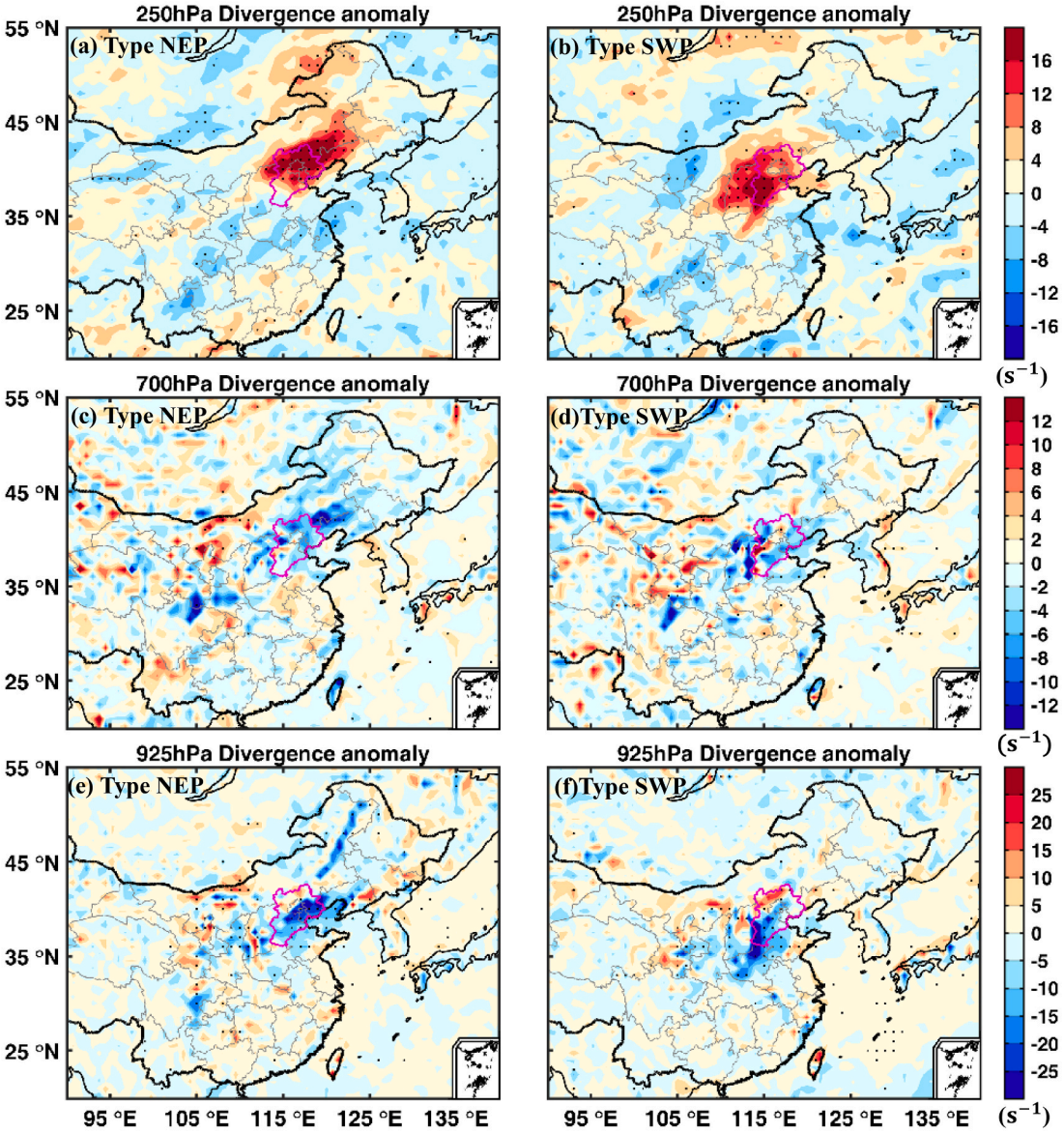

Fig. 8. Composite charts of the anomalies of divergence (unit: s^{-1}) associated with the two types of summer extreme precipitation in BTH. The left and right columns respectively show the anomalies associated with *Type NEP* and *Type SWP*. The top, middle, and bottom rows show the anomalies at 250-, 700-, and 925 hPa, respectively. Black scatter point indicates anomalies significant at the 0.05 level (two-tailed Student's t-test). The boundary of BTH is indicated by the thick purple outline. (For interpretation of the references to colour in this figure legend, the reader is referred to the web version of this article.)

southwestern BTH, which strengthen the ascending motion for extreme precipitation (Fig. 8b and f).

3.3.3. Moisture conditions associated with two types of extreme precipitation

The key factors for triggering rainstorms include not only the strong convective activity induced by atmospheric circulations but also sufficient water vapor conditions. Thus, we also examine the vertically integrated moisture fluxes and the vertically integrated moisture transport at four boundaries of BTH associated with the two types of extreme precipitation to reveal the underlying mechanisms of summer extreme precipitation in BTH from the perspective of water vapor. For the two types of extreme precipitation, we find the transport and accumulation of moisture over BTH are obviously modulated by the atmospheric circulations as the spatial distribution of the anomalous vertically integrated moisture fluxes (Fig. 9a and b) is similar to the spatial distribution of wind vectors at 850 hPa (Fig. 7e and f). Notably, the significant anomalous southerly airflows cover over the BTH for the both extreme precipitation types and thus strengthen the water vapor transport from the southern boundaries of BTH to the precipitation centers (Fig. 9). As a result, the incoming (outgoing) moisture transport exists at the southern (northern) boundary of BTH for the both extreme precipitation types. In addition to the observed similarities in moisture transport between the two precipitation types, the differences observed are also obvious and discussed as below.

In the case of *Type NEP*, under the effects of the western low- and eastern high-pressure systems over BTH, the significant anomalous southwesterly and southerly airflows strengthen the water vapor transports from South China and west of BTH to the northeastern BTH. As a result, a large amount of moisture converges over northeastern BTH (Fig. 9c) by the two incoming channels of water vapor existing at the southern ($8.85 \times 10^7 kg/s$) and western ($2.88 \times 10^7 kg/s$) boundaries of BTH (Fig. 9a). Moreover, the intensity of incoming moisture transport is much stronger than that of outgoing moisture transport existing at the northern and eastern boundaries of BTH (Fig. 9a), resulting in about $5.15 \times 10^7 kg/s$ anomalous water vapor flux cumulating over the

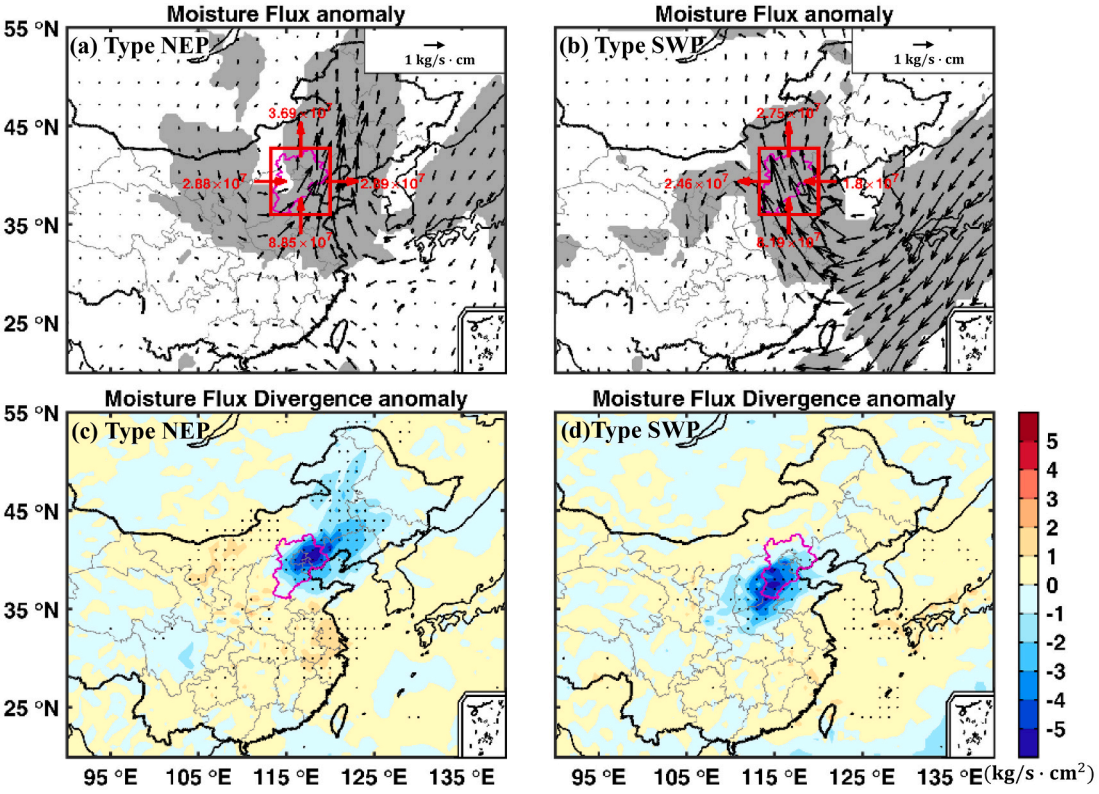

Fig. 9. Composite charts of the anomalies of vertically integrated moisture fluxes(unit: kg/s • cm) and vertically integrated moisture flux divergence (unit: kg/s • cm^2) associated with the two types of summer extreme precipitation in BTH. The left and right columns respectively show the anomalies associated with *Type NEP* and *Type SWP*. The top and bottom rows show the anomalies of vertically integrated moisture fluxes and vertically integrated moisture flux divergence, respectively. Black scatter point indicates anomalies significant at the 0.05 level (two-tailed Student's t-test). The boundary of BTH is indicated by the thick purple outline. (For interpretation of the references to colour in this figure legend, the reader is referred to the web version of this article.)

northeastern BTH (Fig. 9a and c) and corresponding to the precipitation center of *Type NEP*. These results highlight that the atmospheric circulation supplies sufficient moisture for the occurrence of *Type NEP* extreme precipitation by modulating water vapor incoming and outgoing moisture transport channels.

Compared with the extreme precipitation of *Type NEP*, the spatial distribution of water vapor transport associated with the extreme precipitation of *Type SWP* exhibits obvious differences. The strong anomalous of southerly (easterly) airflows (Fig. 7f) induced by the anomalous low-pressure (high-pressure) systems respectively covering over the southwest (northeast) of BTH (Fig. 6f), strengthening the water vapor transports from southern (eastern) boundaries of BTH to the southeastern BTH (Fig. 9b). As a result, two incoming channels of moisture at the southern (8.19×10^7kg/s) and eastern (1.8×10^7kg/s) boundaries are observed in Fig. 9b. It is noteworthy that the total incoming moisture is much larger that the outgoing moisture from the two moisture transport channels at the northern and western boundaries of BTH (Fig. 9b). Thus, the cumulative amount of anomalous water vapor flux about 4.78×10^7kg/s from the four boundaries of BTH indicate net water vapor inflows to BTH (Fig. 9b) and converge over southwestern BHT (Fig. 9d) that corresponds to precipitation center. These results suggest that the obvious differences in the incoming and outgoing channels of moisture transport induced by atmospheric circulations play a key role in determining the differences in the spatial distribution of the two types of summer extreme precipitation in BTH.

3.3.4. *Vertical structures associated with two types of extreme precipitation*

To improve our understanding of the dynamic conditions for triggering two types of extreme precipitation in BTH, the atmospheric vertical structures in the troposphere are also examined. The composite vertical-zonal cross-sections of the anomalies of geopotential height and vertical velocity averaged along the zone between 112.5° and 120.75°E are depicted in Fig. 10. The vertical structure of atmospheric circulation associated with *Type NEP* is shown in Fig. 10a and we find a significant anomaly low-pressure (high-pressure) exist over BTH from surface to 600 hPa (from 600 hPa to 50 hPa). The lower-level (upper-level) cyclonic system (anticyclonic system) respectively induce convergence (divergence) in the lower-troposphere (upper-troposphere) and then jointly trigger ascending motion over BTH. As a result, the significant anomaly ascending motion is observed in the whole troposphere over the northern BTH (Fig. 10c). It's also noteworthy that the significant anomaly descending motion is observed over the zone between 25° to 35°N in the south of BHT, which forms a vertical circulation structure together with the anomaly ascending motion over BTH (Fig. 10c) and is benefit to the maintaining of the ascending motion over BTH. These results further highlight that the vertical structures of geopotential height and vertical velocity in the troposphere provide favorable dynamical conditions for the occurrence of *Type NEP* extreme precipitation by enhancing convective activities with ascending motion.

Compared with *Type NEP*, a significant anomaly low-pressure (high-pressure) system is also observed in the lower-troposphere (upper-troposphere) (Fig. 10b) in *Type SWP*. In contrast, the lower-pressure (upper-pressure) system respectively cover over the south (north) of BTH. As a result, a convergent flow induced by the two synoptic systems exists in the whole troposphere over the southern BTH, thus inducing strong convective activities there. As shown in Fig. 10d, an anomalous ascending air column is observed over the southern BTH, providing the favorable dynamical conditions of triggering extreme precipitation in the southwestern BTH. These results suggest that the obvious differences in the vertical structures of geopotential height and vertical velocity in

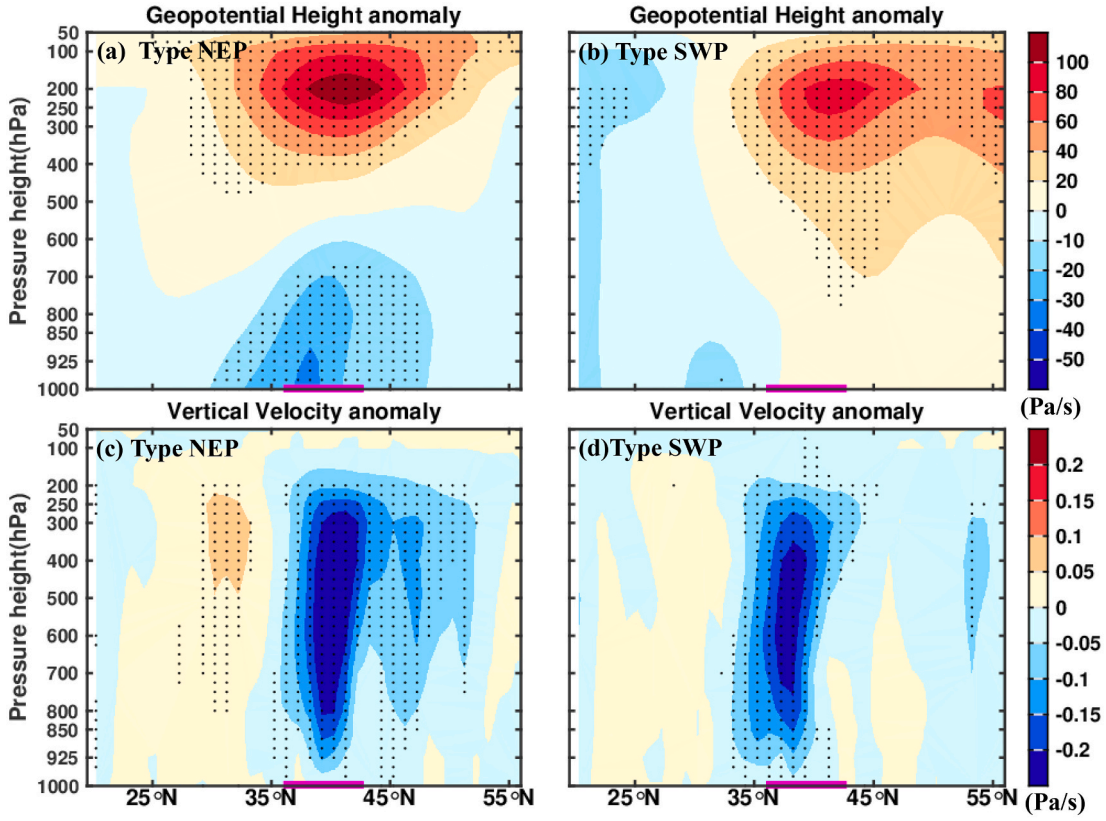

Fig. 10. Composite vertical-latitudinal cross-sections of the anomalies of geopotential height (unit: gpm) and vertical velocity (unit: Pa/s) associated with the two types of summer extreme precipitation in BTH. The left and right columns respectively show the anomalies associated with *Type NEP* and *Type SWP*. The top and bottom rows show the anomalies of geopotential height and vertical velocity, respectively. Black scatter point indicates anomalies significant at the 0.05 level (two-tailed Student's t-test). The boundary of BTH is indicated by the thick purple outline. (For interpretation of the references to colour in this figure legend, the reader is referred to the web version of this article.)

the troposphere also play a key role in determining the differences in the spatial distribution of the two types of summer extreme precipitation in BTH by modulating dynamical conditions.

4. Discussions

Summer extreme precipitation events are widely investigated and most of current studies identify the extreme precipitation event by the definition of precipitation indices including the relative threshold method (Karl et al., 1999; Zhou et al., 2014; Sui et al., 2018; Dong et al., 2021). The identified extreme precipitation events represent 'the normality of extreme values' (Li and Yang, 2015) with relatively high occurrence frequency (Liu, 2022)u and are not enough to capture the most extreme precipitation condition. For example, the extreme precipitation events even identified by the 99th percentile relative thresholds in wet climate area may also occur more than once per year (Dong et al., 2021) and thus cannot depict the tremendously heavy precipitation events. However, the tremendously heavy precipitation events that occur every few years in BTH could exert serious damages to people's safety and cause huge economic losses (Nanding et al., 2020; Ren et al., 2020; Huang et al., 2018b). To capture the most extreme precipitation condition, we select the GEV distribution theory to identify summer extreme precipitation in BTH and examine their long-term changes in this study. We find that the regional summer extreme precipitation days with $>$ 10 years return period exhibit significantly increasing trends in Beijing-Tianjin and surrounding urban areas, indicating that tremendously heavy precipitation events tend to occur frequently in urban areas and bring greater loss of life and finances to humanity. Therefore, it is of great significance to investigate the underlying physical mechanism of the tremendously heavy precipitation events in BTH.

Currently, the underlying mechanisms of summer extreme precipitation events are widely revealed by examining the physical processes of all extreme precipitation events as a whole, rather than performing cluster analysis (Ning et al., 2021; Huang et al., 2017). For instance, the summer extreme precipitation in East China is affected by the weak EASM and the southerly strong WPSH (Wang and Zhou, 2005; Qian et al., 2009; Lu et al., 2004). However, the summer extreme precipitation in North China is significantly modulated by the circulation pattern of western low-pressure and eastern high-pressure system (Chen, 2012; Liu et al., 2007), accompanying with water vapor transport by strengthened EASM (Ding, 1992; Li and Zhou, 2015) and northward-extended WPSH (Wang and Zhou, 2005). Notably, the spatial distributions of different summer extreme precipitation events in the same region also exhibit distinct differences and may be modulated by different underlying mechanisms. In this study, the regional extreme precipitation events in BTH are objectively divided into *Type NEP* and *Type SWP* according to their spatial distribution and the diverse circulation patterns and moisture transports for the two types of precipitation are also revealed. For the *Type NEP*, the anomalous low-pressure (high-pressure) systems respectively cover over the west (east) of BTH, which jointly induce strong anomalous southwesterly and southerly airflows converging over BTH. The converging airflows transport large amount of water vapor to northeastern BTH and induce strong convection over here, thereby triggering extreme precipitation of *Type NEP*. In contrast, the extreme precipitation of *Type SWP* is characterized by the deep (shallow) anomalous high-pressure (low-pressure) systems respectively cover over northeast (southwest) of BTH. The spatial pattern of the two systems induces strong anomalous southerly and easterly airflows and transport large amount of moisture to southwestern BTH. These findings highlight that extreme precipitation events in BTH, which belongs to the

extratropical area are significantly affected by the spatial patterns of atmospheric circulations and moisture transport. Notably, the link between atmospheric moisture transport and extreme precipitation at global scale is examined by Gimeno-Sotelo and Gimeno, 2023. They found that the relationship between moisture transport and extreme daily precipitation is very weak or even negligible in tropical regions, while the moisture transport strongly influences extreme precipitation in extratropical regions (Gimeno-Sotelo and Gimeno, 2023). Thus, our results are highly consistent with context of how moisture transport affects extreme precipitation globally (Gimeno-Sotelo and Gimeno, 2023) and could provide evidence from the observational perspective.

5. Conclusion

In this study, we have selected the GEV distribution theory and K-means clustering method to identify and examine the changes and underlying mechanisms of summer extreme precipitation events in BTH. The major findings are concluded as below. In BTH, summer extreme precipitation days exhibit significantly increasing trends and the increasing rates are more rapid in the urban areas than these in the rural areas, indicating that summer extreme precipitation events become more and more frequent and the urban areas face greater disaster risk of rainstorm. Moreover, the regional summer extreme precipitation events are divided into two types according to the spatial distribution by K-means clustering method: Northeast precipitation (*Type NEP*) and Southwest precipitation (*Type SWP*). Schematic diagrams of physical mechanisms associated with the two types of summer extreme precipitation in BTH are shown in Fig. 11. In the case of *Type NEP*, the anomalous deep low-pressure (high-pressure) systems respectively cover over the west (east) of BTH, which jointly induce strong anomalous southwesterly and southerly airflows converging over BTH (Fig. 11a). The converging airflows strengthen water vapor transports from the western and southern boundaries of BTH and result in a strong convection over northeastern BTH, thereby triggering *Type NEP* precipitation (Fig. 11a). Compared with *Type NEP*, the circulation pattern of *Type SWP* is characterized by the deep (shallow) anomalous high-pressure (low-pressure) systems respectively covering over northeast (southwest) of BTH, which induce strong anomalous southerly and easterly airflows converging over BTH, thereby strengthening the water vapor transports from the southern and eastern boundaries of BTH and finally resulting in a strong convection over southwestern region of BTH (Fig. 11b).

Our study is critical to improve our understanding of the underlying physical mechanism of summer extreme precipitation in BTH. These findings lay a theoretical foundation for the improvement of extreme precipitation forecast and provide scientific insights for preventing the disaster caused by extreme precipitation over here.

CRediT authorship contribution statement

Jing Cong: Writing – original draft, Validation, Software, Investigation, Formal analysis, Data curation. **Huijun Liu:** Writing – review & editing, Methodology, Investigation. **Guicai Ning:** Writing – review & editing, Supervision, Resources, Project administration, Methodology, Formal analysis, Conceptualization. **Hong Chen:** Writing – review & editing, Software, Investigation. **Xueyan Bi:** Writing – review & editing,

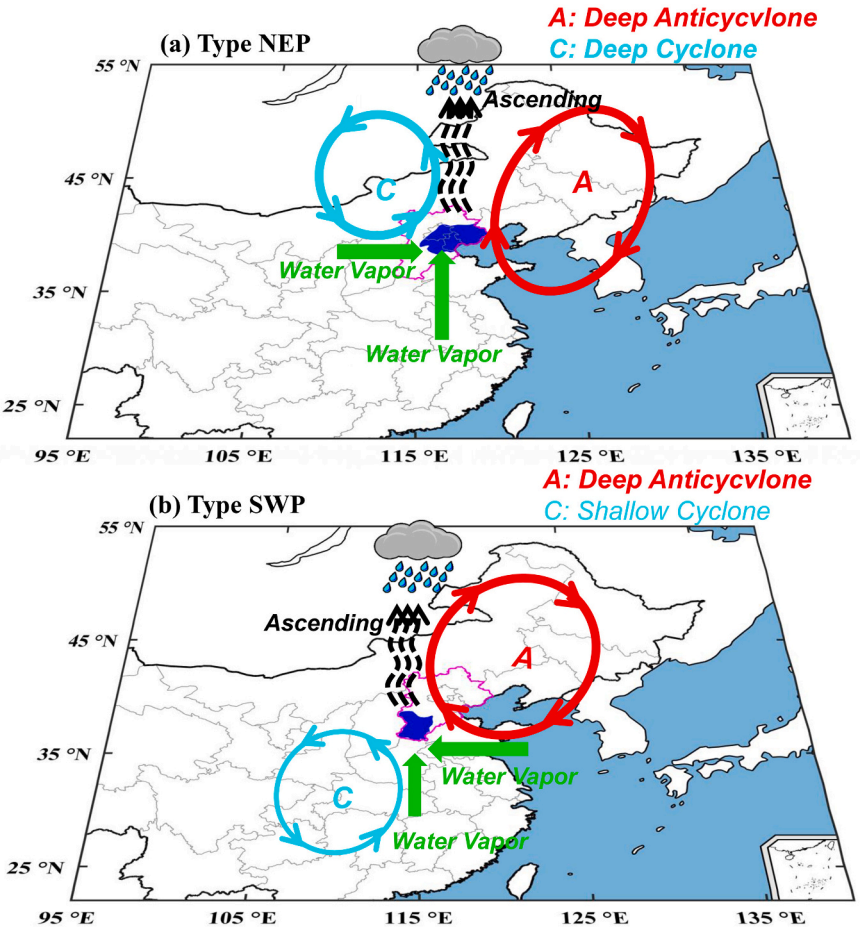

Fig. 11. Schematic diagrams of physical mechanisms associated with the two types of summer extreme precipitation in BTH. The top and bottom rows show schematic diagram associated with *Type NEP* and *Type SWP*.

Investigation. **Bo Liu:** Writing – review & editing, Investigation. **Yuanjian Yang:** Writing – review & editing, Investigation. **Haiyun Xia:** Writing – review & editing, Investigation.

Declaration of competing interest

The authors declare that they have no known competing financial interests or personal relationships that could have appeared to influence the work reported in this paper.

Data availability

Data will be made available on request.

Acknowledgments

This study is funded by the Startup Foundation for Introducing Talent of NUIST (2023r005), the Open Project of Fujian Key Laboratory of Severe Weather (2021KFKT05), and the Bohai Rim Regional Meteorological Science and Technology Collaborative Innovation Fund Project (QYXM202208). The authors are thankful to the observed meteorological data provided by China Meteorological Administration (CMA) and ERA5 hourly reanalysis data provided by European Centre for Medium-Range Weather Forecasts (ECMWF). The authors also thank the High Performance Computing Center of Nanjing University of Information Science & Technology for their support of this work. We are thankful to the anonymous reviewers who provided valuable comments and suggestions.

Appendix A. Supplementary data

Supplementary data to this article can be found online at https://doi.org/10.1016/j.atmosres.2024.107304.

References

Ahasan, M.N., Chowdhury, M.A.M., Quadir, D.A., 2013. Simulation of high impact rainfall events over southeastern hilly region of Bangladesh using MM5 model. Int. J. Atmos. Sci. 2013, 1–13. https://doi.org/10.1155/2013/657108.

Akaike, H., 1974. A new look at the statistical model identification. IEEE Trans. Autom. Control 19 (6), 716–723. https://doi.org/10.1007/978-1-4612-1694-0_16.

Bernier, C., Wang, Y., Estes, M., et al., 2019. Clustering surface ozone diurnal cycles to understand the impact of circulation patterns in Houston, TX. J. Geophys. Res.-Atmos. 124 https://doi.org/10.1029/2019JD031725.

Caliński, T., Harabasz, J., 1974. A dendrite method for cluster analysis. Commun. Stat. 3, 1–27. https://doi.org/10.1080/03610927408827101.

Chen, X., 2012. Studies on the Characteristics and Formative Cause of Extreme Precipitation Events in the Northern China. Master thesis. Lanzhou University, China.

Chen, Y., Sun, J., Xu, J., et al., 2012. Analysis and thinking on the extremes of the 21 July 2012 torrential rain in Beijing PartI: observation and thinking. Meteorol. Mon. 38 (10), 1255–1266. https://doi.org/10.7519/J.ISSN.1000-0526.2012.10.012 (in Chinese).

Chikumbo, O., Granville, V., 2019. Optimal clustering and cluster identity in understanding high-dimensional data spaces with tightly distributed points. Mach. Learn. Knowl. Extract. 1 (2), 715–744. https://doi.org/10.3390/make1020042.

Coles, S., 2001. An Introduction to Statistical Modeling of Extreme Values. Springer, London, UK. ISBN: 1852334592, 208 pp.

Cressie, N., 1980. Relaxing assumptions in the one sample t-test. Aust. J. Stat. 22 (2), 143–153. https://doi.org/10.1111/j.1467-842x.1980.tb01161.x.

Darby, L.S., 2005. Cluster analysis of surface winds in Houston, Texas, and the impact of wind patterns on ozone. J. Appl. Meteorol. 44 (12), 1788–1806. https://doi.org/10.1175/jam2320.1.

Ding, Y., 1992. Summer monsoon rainfalls in China. J. Meteorol. Soc. Jpn. Ser. II 70 (1B), 373–396. https://doi.org/10.2151/jmsj1965.70.1b_373.

Donat, M.G., Lowry, A.L., Alexander, L.V., et al., 2016. More extreme precipitation in the world's dry and wet regions. Nat. Clim. Chang. 6, 508–513. https://doi.org/10.1038/nclimate2941.

Dong, S., Sun, Y., Li, C., et al., 2021. Attribution of extreme precipitation with updated observations and CMIP6 simulations. J. Clim. 34 (3), 871–881. https://doi.org/10.1175/JCLI-D-19-1017.1.

Du, J., Grumm, R.H., Deng, G., 2014. Ensemble anomaly forecasting approach to predicting extreme weather demonstrated by extremely heavy rain event in Beijing. Chin. J. Atmos. Sci. 38 (4), 685–699. https://doi.org/10.3878/j.issn.1006-9895.2013.13218 (in Chinese).

Easterling, D.R., Evans, J.L., Groisman, P.Y., et al., 2000. Observed variability and trends in extreme climate events: a brief review. Bull. Am. Meteorol. Soc. 81 (3), 417–425. https://doi.org/10.1175/1520-0477(2000)0812.3.CO;2.

Gao, X., 2020. Research on Improved K-Means Algorithm and New Cluster Validity Index. Master thesis. Anhui University, China.

Gimeno-Sotelo, L., Gimeno, L., 2023. Where does the link between atmospheric moisture transport and extreme precipitation matter? Weather Clim. Extrem. 39, 100536, 100536.10.1016/j.wace.2022.100536.

Guo, J., Xiong, M., Huang, H., 2019. Analysis of diurnal variation characteristics of rainfall during warm season in Beijing-Tianjin-Hebei region. J. Mar. Meteorol. 39 (2), 58–67. https://doi.org/10.19513/j.cnki.issn2096-3599.2019.02.006 (in Chinese).

Hartmann, H., Buchanan, H., 2014. Trends in extreme precipitation events in the Indus River Basin and flooding in Pakistan. Atmosphere-Ocean 52 (1), 77–91. https://doi.org/10.1080/07055900.2013.859124.

Hersbach, H., Bell, B., Berrisford, P., et al., 2020. The ERA5 global reanalysis. Q. J. R. Meteorol. Soc. 146 (730), 1999–2049. https://doi.org/10.1002/qj.3803.

Hong, G., 2020. Localized revision and application of assessing indices for regional heavy rainfall events in Hubei Province. Torrential Rain Disasters 39 (5), 470–476. https://doi.org/10.3969/j.issn.1004-9045.2020.05.005 (in Chinese).

Hu, H., Li, L., Wang, J., et al., 2018. A case study on the heavy rainfall in Shaanxi-Gansu-Ningxia and associated atmospheric circulations and water vapor channels in 2016. J. Arid Meteorol. 36 (5), 776–781. https://doi.org/10.11755/j.issn.1006-7639(2018)-05-0776 (in Chinese).

Huang, W., Chang, S., Xie, C., Zhang, Z., 2017. Moisture sources of extreme summer precipitation events in North Xinjiang and their relationship with atmospheric circulation. Adv. Clim. Chang. Res. 8 (1), 12–17. https://ir.lzu.edu.cn/handle/262010/193296.

Huang, T., Gao, P., Wu, A., et al., 2018a. Research on the numerical simulation of heavy rain in Guizhou mountains based on WRF model. Mid-Low Latitude Mt. Meteorol. 42 (4), 8–15 (in Chinese) CNKI:SUN:GZQX.0.2018-04-002.

Huang, D., Zhang, L., Gao, G., et al., 2018b. Projected changes in population exposure to extreme heat in China under a RCP8.5 scenario. J. Geogr. Sci. 28 (10), 1371–1384. https://doi.org/10.1007/s11442-018-1550-5.

IPCC, 2021. Climate Change 2021: The Physical Science Basis. Contribution of Working Group I to the Sixth Assessment Report of the Intergovernmental Panel on Climate Change. Cambridge University Press. https://doi.org/10.1017/9781009157896.

Jain, A.K., Murty, M.N., Flynn, P.J., 1999. Data clustering: a review. ACM Comput. Surv. 31 (3), 264–323. https://doi.org/10.1145/331499.331504.

Jin, D., 2014. Variations and the Extreme of Regional Rainfall in East China during Boreal Summer: Phenomena and Mechanisms. PHD thesis. Nanjing University of Information Science & Technology, China.

Kang, Y., 2017. A Study on Numerical Simulation and Diagnostic Analysis on the Torrential Rainfall Event in North China during 18–21 July, 2016. Master thesis. Lanzhou University, China.

Karl, T.R., Nicholls, N., Ghazi, A., 1999. CLIVAR/GCOS/WMO workshop on indices and indicators for climate extremes: workshop summary. Clim. Chang. 42 (1), 3–7. https://doi.org/10.1023/A:1005491526870.

Kendall, M., 1975. Rank Correlation Methods. Charles Griffin, London.

Li, M., 2011. Spatial and Temporal Features of Precipitation Extremes in Association with Circulation Changes in Eastern China over the Past Five Decades. Master thesis. Nanjing University of Information Science & Technology, China.

Li, Y., Yang, C., 2015. Non-stationary modeling and trend analysis of return levels of climate extremes in China. Clim. Environ. Res. 20 (3), 347–355. https://doi.org/10.3878/j.issn.1006-9585.2015.14246 (in Chinese).

Li, R.C.Y., Zhou, W., 2015. Multiscale control of summertime persistent heavy precipitation events over South China in association with synoptic, intraseasonal, and low-frequency background. Clim. Dyn. 45 (3–4), 1043–1057. https://doi.org/10.1007/s00382-014-2347-6.

Li, X., Fan, K., Xu, Z., 2019. Decrease in extreme precipitation in summer over East Northern China and the water-vapor transport characteristics after year 2000. Chin. J. Atmos. Sci. 43 (5), 1109–1124. https://doi.org/10.3878/j.issn.1006-9895.1902.18198 (in Chinese).

Liang, S., Cheng, S., Hao, L., et al., 2018. Analysis on the characteristics of hourly precipitation variations in Beijing-Tianjin-Hebei region during 1970-2015. Torrential Rain Disasters 37 (2), 105–114. https://doi.org/10.3969/j.issn.1004-9045.2018.02.002 (in Chinese).

Liu, H., Wang, W., Shao, M., et al., 2007. A case study of the influence of the Western Pacific Subtropical High on the torrential rainfall in Beijing Area. Chin. J. Atmos. Sci. 31 (4), 727–734 (in Chinese).

Liu, Y., 2022. Projected Change on Multi-Year Annual Extreme of Daily Heat and Precipitation Events in China. Master thesis. East China Normal University, China.

Long, Y., Fan, G., Duan, L., et al., 2016. A study on the characteristics of summertime extreme precipitation events over China in recent 54 years. Clim. Environ. Res. 21 (4), 429–438. https://doi.org/10.3878/j.issn.1006-9585.2016.15130 (in Chinese).

Lu, J., Ren, J., Ju, J., 2004. The interdecadal variability of East Asia monsoon and its effect on the rainfall over China. J. Trop. Meteorol. 20 (1), 73–80. https://doi.org/10.16032/j.issn.1004-4965.2004.01.008 (in Chinese).

Łukasik, S., Kowalski, P.A., Charytanowicz, M., et al., 2016. Clustering using flower pollination algorithm and Calinski-Harabasz index. In: 2016 IEEE Congress on Evolutionary Computation (CEC), Vancouver, BC, Canada, pp. 2724–2728. https://doi.org/10.1109/CEC.2016.7744132.

Luo, M., Lau, N.-C., 2017. Heat waves in southern China: synoptic behavior, long-term change, and urbanization effects. J. Clim. 30 (2), 703–720. https://doi.org/10.1175/JCLI-D-16-0269.1.

Luo, M., Ning, G., Xu, F., et al., 2020. Observed heatwave changes in arid Northwest China: physical mechanism and long-term trend. Atmos. Res. 242, 105009 https://doi.org/10.1016/j.atmosres.2020.105009.
MacQueen, J., 1967. Some methods for classification and analysis of multivariate observations. In: Proceedings of the fifth Berkeley Symposium on Mathematical Statistics and Probability, pp. 281–297.
Mann, H., 1945. Nonparametric tests against trend. Econometrica 13 (3), 245–259. https://doi.org/10.2307/1907187.
Nanding, N., Chen, Y., Wu, H., et al., 2020. Anthropogenic influences on 2019 July precipitation extremes over the mid-lower reaches of the Yangtze River. Front. Environ. Sci. 8, 603061. https://doi.org/10.3389/fenvs.2020.603061.
Ning, G., Luo, M., Zhang, Q., et al., 2021. Understanding the mechanisms of summer extreme precipitation events in Xinjiang of arid Northwest China. J. Geophys. Res. Atmos. 126 (15), e2020JD034111 https://doi.org/10.1029/2020JD034111.
Pingale, S., Khare, D., Jat, M., et al., 2016. Trend analysis of climatic variables in an arid and semi-arid region of the Ajmer District, Rajasthan, India. J. Water Land Dev. 28 (I-III), 3–18. https://doi.org/10.1515/jwld-2016-0001.
Qian, D., Guan, Z., Wang, L., 2009. Interdecadal variations of West Pacific Subtropical High area and changes in summer precipitation over China in Boreal summer during the last 57 years. Trans. Atmos. Sci. 32 (5), 677–685 (in Chinese) CNKI:SUN:NJQX.0.2009-05-011.
Quan, R.-S., 2014. Rainstorm waterlogging risk assessment in central urban area of Shanghai based on multiple scenario simulation. Nat. Hazards. 73 (3), 1569–1585. https://doi.org/10.1007/s11069-014-1156-x.
Rawlins, M.A., Steele, M., Holland, M.M., et al., 2010. Analysis of the Arctic system for freshwater cycle intensification: observations and expectations. J. Clim. 23 (21), 5715–5737. https://doi.org/10.1175/2010JCLI3421.1.
Ren, L., Wang, D., An, N., et al., 2020. Anthropogenic influences on the persistent night-time heat wave in summer 2018 over Northeast China. Bull. Am. Meteorol. Soc. 101 (1), S83–S88. https://doi.org/10.1175/BAMS-D-19-0152.1.
Saeed, S., Müller, W.A., Hagemann, S., et al., 2011. Circumglobal wave train and the summer monsoon over northwestern India and Pakistan: the explicit role of the surface heat low. Clim. Dyn. 37, 1045–1060. https://doi.org/10.1007/s00382-010-0888-x.
Sang, Y., Wang, Z., Liu, C., 2014. Comparison of the MK test and EMD method for trend identification in hydrological time series. J. Hydrol. 510, 293–298. https://doi.org/10.1016/j.jhydrol.2013.12.039.
Seneviratne, S.I., Nicholls, N., Easterling, D., et al., 2012. Changes in climate extremes and their impacts on the natural physical environment. In: Managing the Risks of Extreme Events and Disasters to Advance Climate Change Adaptation: Special Report of the Intergovernmental Panel on Climate Change. Cambridge University Press, pp. 109–230. https://doi.org/10.1017/CBO9781139177245.006.
Stephenson, A.G., 2018. Original S functions written by Janet E. Heffernan with R port and R documentation provided by Alec G. Stephenson. ismev: An Introduction to Statistical Modeling of Extreme Values. R package version 1.42.
Sui, Y., Lang, X., Jiang, D., 2018. Projected signals in climate extremes over China associated with a 2 °C global warming under two RCP scenarios. Int. J. Climatol. 38 (S1), e678–e697. https://doi.org/10.1002/joc.5399.
Sun, J., Zhang, F., 2017. Daily extreme precipitation and trends over China. Sci. China Earth Sci. 60, 2190–2203. https://doi.org/10.1007/s11430-016-9117-8.
Sun, Q., Zhang, X., Zwiers, F.W., et al., 2020. A global, continental, and regional analysis of changes in extreme precipitation. J. Clim. 34 (1), 243–258. https://doi.org/10.1175/JCLI-D-19-0892.1.
Tu, K., Yan, Z., Fan, L., et al., 2022. Study of evaluation method on the climate of extreme high temperatures based on dynamic return periods. Clim. Chang. Res. 19 (1), 11–22. https://doi.org/10.12006/j.issn.1673-1719.2022.008 (in Chinese).
Wang, Y., Zhou, L., 2005. Observed trends in extreme precipitation events in China during 1961-2001 and the associated changes in large-scale circulation. Geophys. Res. Lett. 32 (9), L09707. https://doi.org/10.1029/2005GL22574.
Wang, H., Gao, T., Xie, L., 2019. Extreme precipitation events during 1960–2011 for the Northwest China: space-time changes and possible causes. Theor. Appl. Climatol. 137, 977–995. https://doi.org/10.1007/s00704-018-2645-8.
Westra, S., Alexander, L.V., Zwiers, F.W., 2013. Global increasing trends in annual maximum daily precipitation. J. Clim. 26 (11), 3904–8918. https://doi.org/10.1175/JCLI-D-12-00502.1.
Wu, J., Zhou, B.-T., Xu, Y., 2015. Response of precipitation and its extremes over China to warming: CMIP5 simulation and projection. Chin. J. Geophys. 58 (5), 461–473. https://doi.org/10.1002/cjg2.20187.
Xie, K., Ren, X., 2008. Climatological characteristics of atmospheric water vapor transport and its relation with rainfall over North China in summer. J. Meteorol. Sci. 28 (5), 508–514. https://doi.org/10.3969/j.issn.1009-0827.2008.05.006 (in Chinese).
Xu, Y., Gao, X., Giorgi, F., 2009. Regional variability of climate change hot-spots in East Asia. Adv. Atmos. Sci. 26 (4), 783–792. https://doi.org/10.1007/s00376-009-9034-2.
Yan, G., 2013. Study on the Impact of Taihang Mountains on Torrential Rains in North China. PHD thesis. Nanjing University of Information Science & Technology, China.
Yu, W., Wu, Z., He, Q., et al., 2015. Weather Forecasting Method Handbook for Tianjin, 1th ed. China Meteorological Press, Beijing (in Chinese).
Zaz, S.N., Romshoo, S.A., Krishnamoorthy, R.T., et al., 2019. Analyses of temperature and precipitation in the Indian Jammu and Kashmir region for the 1980-2016 period: implications for remote influence and extreme events. Atmos. Chem. Phys. 19 (1), 15–37. https://doi.org/10.5194/acp-19-15-2019.
Zhai, P.M., Zhang, X.B., Wan, H., et al., 2005. Trends in total precipitation and frequency of daily precipitation extremes over China. J. Clim. 18 (7), 1096–1108. https://doi.org/10.1175/JCLI-3318.1.
Zhang, W., Zhou, T., 2020. Increasing impacts from extreme precipitation on population over China with global warming. Sci. Bull. 65 (3), 243–252. https://doi.org/10.1016/j.scib.2019.12.002.
Zhao, Y., Xu, X., Li, J., et al., 2019. The large-scale circulation patterns responsible for extreme precipitation over the North China Plain in midsummer. J. Geophys. Res. Atmos. 124 (23), 12794–12809. https://doi.org/10.1029/2019JD030583.
Zhou, X., Ding, Y., Wang, P., 2008. Features of moisture transport associated with the precipitation over North China during July-August. Chin. J. Atmos. Sci. 32 (2), 345–357. https://doi.org/10.3878/j.issn.1006-9895.2008.02.13.
Zhou, B., Wen, Q., Xu, Y., et al., 2014. Projected changes in temperature and precipitation extremes in China by the CMIP5 multimodel ensembles. J. Clim. 27 (17), 6591–6611. https://doi.org/10.1175/JCLI-D-13-00761.1.
Zhou, Y., Sun, D., Zhao, Y., et al., 2021. Characteristics of wide-range extreme precipitation in summer and its circulation anomalies in Northern Xinjiang. J. Arid Meteorol. 39 (2), 215–224. https://doi.org/10.11755/j.issn,1006-7639(2021)-02-0215 (in Chinese).
Zwiers, F.W., Zhang, X., Feng, Y., 2011. Anthropogenic influence on long return period daily temperature extremes at regional scales. J. Clim. 24 (3), 881–892. https://doi.org/10.1175/2010JCLI3908.1.

Update

Atmospheric Research

Volume 303, Issue , 15 June 2024, Page

DOI: https://doi.org/10.1016/j.atmosres.2024.107333

Atmospheric Research 303 (2024) 107333

Contents lists available at ScienceDirect

Atmospheric Research

journal homepage: www.elsevier.com/locate/atmosres

Corrigendum to "Comparing the mechanisms of two types of summer extreme precipitation in Beijing-Tianjin-Hebei region, China: Insights from circulation patterns and moisture transports" [Atmospheric Research, 302 (2024), 107304]

Jing Cong [a,d], Huijun Liu [c,e], Guicai Ning [b,*], Hong Chen [a,d], Xueyan Bi [f], Bo Liu [a,d], Yuanjian Yang [b], Haiyun Xia [b]

[a] Tianjin Meteorological Observatory, Tianjin 300074, China
[b] Collaborative Innovation Centre on Forecast and Evaluation of Meteorological Disasters, School of Atmospheric Physics, Nanjing University of Information Science & Technology, Nanjing 210044, China
[c] Fujian Key Laboratory of Severe Weather, Fuzhou 350028, China
[d] Tianjin Key Laboratory for Oceanic Meteorology, Tianjin 300074, China
[e] Fujian Provincial Meteorological Observatory, Fuzhou 350028, China
[f] Guangzhou Institute of Tropical and Marine Meteorology, China Meteorological Administration, Guangzhou 510080, China

The authors regret they have identified an error in the Fig. 9.
The correct Fig. 9 should be as follow:

DOI of original article: https://doi.org/10.1016/j.atmosres.2024.107304.
* Corresponding author.
E-mail address: 003746@nuist.edu.cn (G. Ning).

https://doi.org/10.1016/j.atmosres.2024.107333

Available online 13 March 2024

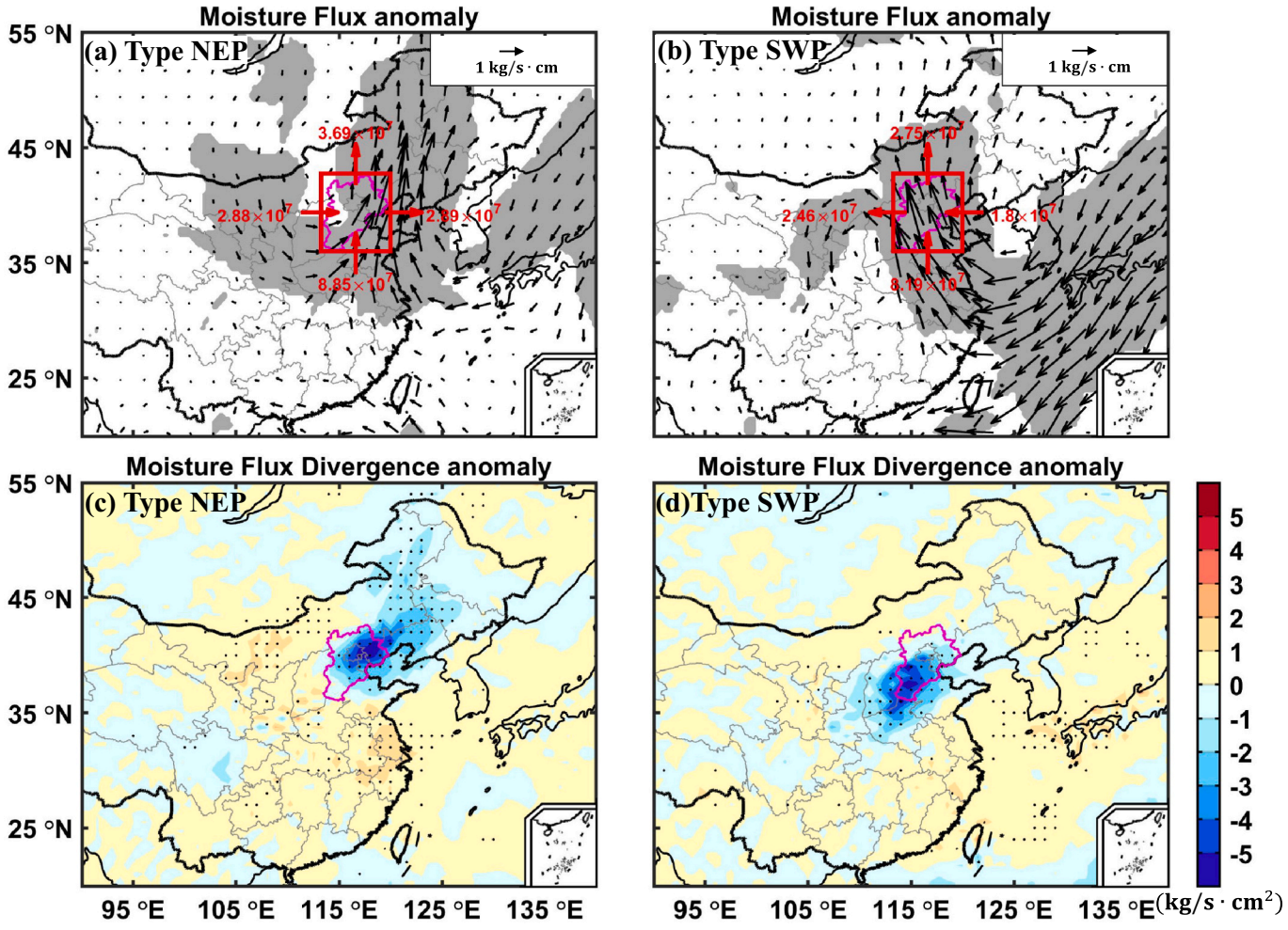

Fig. 9. Composite charts of the anomalies of vertically integrated moisture fluxes (unit: kg/s • cm) and vertically integrated moisture flux divergence (unit: kg/s • cm^2) associated with the two types of summer extreme precipitation in BTH. The left and right columns respectively show the anomalies associated with *Type NEP* and *Type SWP*. The top and bottom rows show the anomalies of vertically integrated moisture fluxes and vertically integrated moisture flux divergence, respectively. Black scatter point indicates anomalies significant at the 0.05 level (two-tailed Student's *t*-test). The boundary of BTH is indicated by the thick purple outline. (For interpretation of the references to colour in this figure legend, the reader is referred to the web version of this article.) (For interpretation of the references to colour in this figure legend, the reader is referred to the web version of this article.)

The authors would like to apologise for any inconvenience caused.